Dissertations, Master's Theses and Master's Reports

2017

FEA ANALYSIS AND OPTIMIZATION OF DIFFERENTIAL HOUSING FOR FATIGUE STRESSES AND FATIGUE TEST DESIGN TO STUDY SKIN EFFECT IN DUCTILE IRON

Swapnil A. Pandey
Michigan Technological University, sapandey@mtu.edu

www.manaraa.com

FEA ANALYSIS AND OPTIMIZATION OF DIFFERENTIAL HOUSING FOR
FATIGUE STRESSES AND FATIGUE TEST DESIGN TO STUDY SKIN EFFECT IN
DUCTILE IRON

By

Swapnil A. Pandey

A REPORT

Submitted in partial fulfillment of the requirements for the degree of

MASTER OF SCIENCE

In Mechanical Engineering

MICHIGAN TECHNOLOGICAL UNIVERSITY

2017

© 2017 Swapnil A. Pandey

This report has been approved in partial fulfillment of the requirements for the Degree of MASTER OF SCIENCE in Mechanical Engineering.

Department of Mechanical Engineering-Engineering Mechanics

Report Advisor: *Dr. Gregory Odegard*

Committee Member: *Dr. Paul Sanders*

Committee Member: *Dr. Timothy Hilditch*

Department Chair: *Dr. William Predebon*

Table of Contents

1

List of figures

3

4

List of tables

List of Symbols

[F] – Force matrix created in FEA

[k] – Stiffness matrix of Finite element model

$\{x\}$ – Nodal displacement vector in static analysis

[M] – Mass matrix of Finite element model

[C] – Damping matrix of Finite element model

$\{\ddot{u}\}$ – Nodal acceleration vector

$\{\dot{u}\}$ – Nodal velocity vector

$\{u\}$ – Nodal displacement vector in transient analysis

$\sigma_{i,a}$ – Alternating normal stress where $i=x,y$ and z directions

$\sigma_{i,m}$ – Mean normal stress where $i=x,y$ and z directions

$\tau_{ij,a}$ – Alternating shear stress where $i,j=x,y$ and z directions

$\tau_{ij,m}$ – Alternating shear stress where $i,j=x,y$ and z directions

$\sigma_{1,max}$ – Maximum principal stress

$\sigma_{3,min}$ – Minimum principal stress

L – Length of the flexural fatigue sample

S – Maximum stress level in the flexural fatigue test

b – Width of the flexural fatigue specimen

d – Thickness of the flexural fatigue sample

P – Load applied on the flexural fatigue sample

E – Young's modulus

f – Displacement value in flexural fatigue test

K_t – Stress concentration factor

7

a – Initial crack depth

c – Initial crack length

K – Stress intensity factor

Y – Geometry shape factor

Φ – Angle of the crack growth direction with loading direction

σ_b – Bending stress in cantilever flexural fatigue sample

y – Distance of surface of sample from neutral axis

M_z – Bending moment in the flexural fatigue sample

I_z – Area moment of inertia of the flexural fatigue sample

Acknowledgements

Abstract

Automotive emission standards are getting more stringent day by day and governments worldwide are moving to reduce emissions from automobiles. In this scenario reducing the weight of automobile components becomes an important design objective to reduce emissions. A 10% reduction of weight in the complete automobile leads to 6-8 percent improvement in mileage (Mhapankar 2015). Also, powertrain components make up for approximately 27% of the total automobile weight and thus optimizing the design of components in the powertrain is an important task (Mhapankar 2015). Statistics show that 26% of component failures in automobiles are part of powertrain and 21% of overall failures are due to design and manufacturing defects (Heyes 1998). Furthermore, more than 90% of design failures are due to fatigue loading rather than static stress failure. The differential design was already optimized using the high Si ductile iron for static stresses by the work done by Mr. Parag Deshpande (Deshpande 2016) and Mr. Pankaj Kalan (Kalan 2016) in this project.

Thus, in this study the new differential design is evaluated for fatigue stresses using a stress life approach. The loading and boundary conditions have been modified from the previous works to better estimate the working condition of the differential case. Time integration of static load cases has been done to obtain fatigue results by running a linear static analysis. FEA models using a quasi-static analysis and transient analysis are compared as a part of the study to select the best possible approach in future applications. The model to use static load cases for fatigue analysis has been compared to standard fatigue solver of Optistruct.

In the second part of the project a flexural fatigue test is designed to study the effects of casting skin and its properties on fatigue life of ductile iron. Sample geometry for the test is designed and updated based on test results. The effects of thickness on the sample behavior and flexural testing is studied. A fracture mechanics approach is proposed to model the crack propagation in ductile iron for crack initiation at the nodules. A preliminary literature study for initiation at other casting defects is done which needs to be expanded and incorporated in the crack growth model.

10

1 Introduction

Weight reduction in automotive components is a a very important design target with the industry moving towards lower emissions and lean designs. Also with automakers making a shift towards electric vehicles, weight optimization of all vehicle systems is an even important factor. This would help increase the miles per charge and decrease the size of battery packs and drive motors used. Thus, the methods developed in this work would help optimizing parts whether for optimizing in-service parts or designing new parts for future projects. For the current study, we are using a pickup truck differential from Eaton as a prototype to establish methods for fatigue analysis of components. The differential was optimized for static stresses in previous works for LIFT project. A weight reduction of 38% using topology optimization in Optistruct. But most of the in service component failures are due to fatigue failure and thus it is important to analyze the design from a fatigue point of view. There is a possibility that the design could be further optimized or some areas would have to be strengthened for dynamic stresses. The geometry in *Figure 1* below gives the exploded view of the differential case provided by Eaton. The primary objective was to optimize the case shown in the figure below.
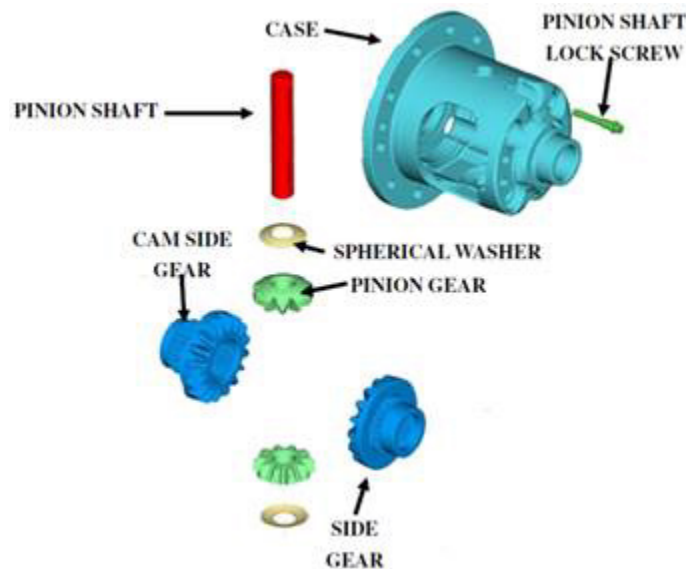
Figure 1 Exploded view of the differential (Klipfel 2016)

11

All the figures shown in this section are taken from report provided by EATON written by David Klipfel. Figure 2 shows the assembled view of the differential with its component. The geometry files for both the differential case and ring gear were provided by EATON. Although the geometry used for this part is the optimized case obtained from the optimized work by Mr. Parag and Mr. Pankaj.
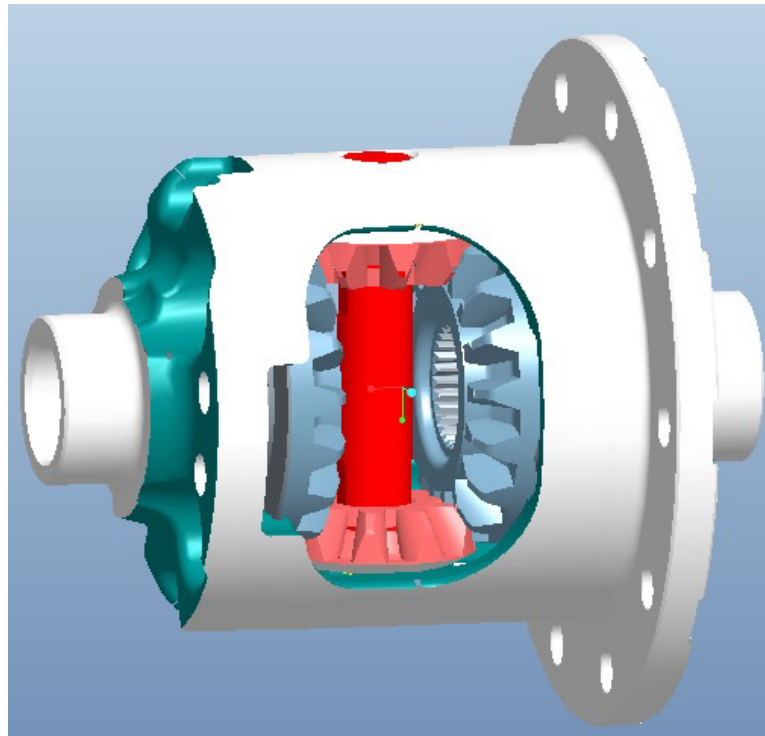
Figure 2 Assembled model of the differential (Klipfel 2016)

1.1 Scope of the project

1.1.1 Fatigue analysis and optimization

The scope of this project is to analyze the optimized differential case design for fatigue performance. A time history of loading for the component is not available, so a method needs to be devised to create a FEA fatigue simulation using the static loading details provided by Eaton. As fatigue is a time dependent dynamic phenomenon and the loading of the component is complex and multiaxial the problem needs to be investigated using two different approaches. The different approaches to be compared are following

1. Quasi-static simulation using independent static cases and integrating
2. Transient simulation

Considering that a new model needs to be developed the original differential design first needs to be analyzed to verify the accuracy of the model by comparing the failure locations in the design and that reported by EATON in their testing. The design also needs to be optimized after analyzing for fatigue stresses. The best approach from the two will be selected for performing the optimization.

1.1.2 Study of effect of casting skin on fatigue properties of ductile iron

The scope of this part of the project is to compare the fatigue properties of inorganic sand binder casting with organic binder sand castings. A flexural fatigue test needs to be designed for a cost effective and quick method to assess samples from both the casting processes. The test would also compare the effect of varying Si and Mn levels in fatigue properties of ductile iron. The primary objective of the project is to compare and study the variation in S-N characteristics due to change in these design variables. However, the deliverables of these projects would be a valuable knowledge addition to improve the fatigue FEA modelling. Firstly, comprehensive fatigue testing would provide us accurate S-N data and thus help to predict life of the component. The comparison of surface profiles and their effect would help in defining the machining for the differential or any component more precisely. Also, if inorganic binder sand is found to have better fatigue performance than other molding sands. It would allow removal of draft angles from the

A sample needs to be designed so that failure during the test is caused purely due to surface condition and skin microstructure and not stress concentrations. Finger mold design and solidification analysis in MAGMA also needs to be completed for sample design. The fracture mechanics model would be further refined as testing progresses and more factors affecting crack initiation and growth are discovered.

13

1.2 Terminology

1.2.1 Differential case regions

The differential is divided into three parts namely

1. Flange side
2. Bell side
3. Barrel region

For this optimization study the whole differential is not considered as the design volume. Initial simulations were done to identify critical locations. Only the regions showing critical damage were selected in the design volume. Also, the regions for mounting of bearings and gears in the differential are excluded from the design volume. The cross-shaft regions also are not considered in the design volume

(a)   *(b)*   *(c)*
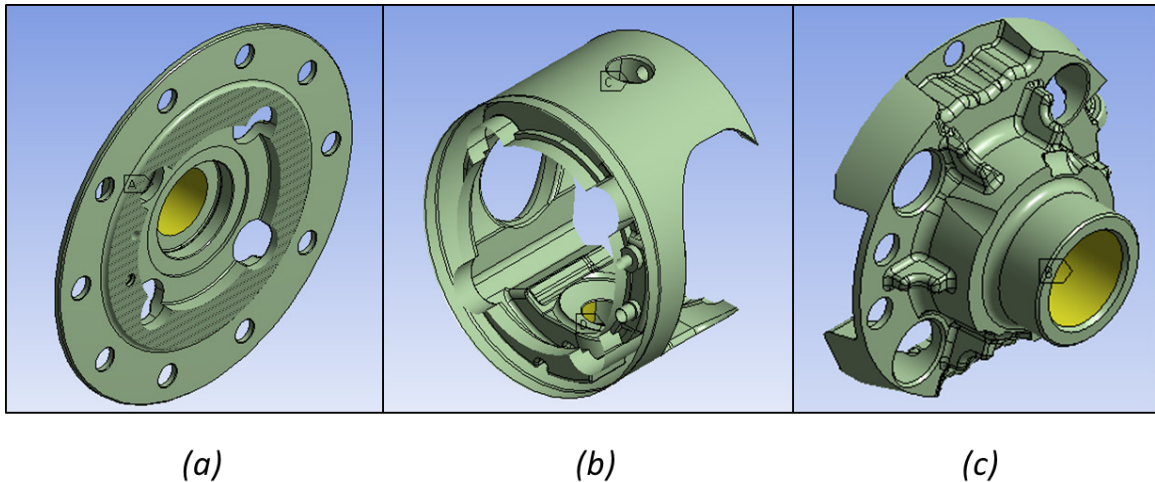
Figure 3 Image showing the three regions of the differential case a) Flange b) Barrell c) Bell region

14

1.2.2 Fatigue sample surfaces

The test designed to gauge the fatigue properties would also compare the effect of surface profiles. The three surface profiles to be studied are

1. Organic binder sand as-cast surface
2. Inorganic binder sand as-cast surface
3. Machined surface

15

2 FEA Preprocessing and Test design

2.1 Preprocessing of differential for Fatigue analysis

2.1.1 Geometry clean up

2.1.1.1 Geometry clean up in ANSYS

The geometry files for differential are imported into the ANSYS Workbench design modeler. The geometry is cleaned up using the automatic clean up tools for repairing seams, sharp angles, slivers, edges and hard edges. The default values in ANSYS for detecting gaps in geometry is 0.37 mm and the same value was used to repair the differential geometry. Due to high number of small surfaces present in the in the geometry, the threshold value for slivers was revised from the default to 1 mm.

2.1.1.2 Geometry clean up in Hypermesh

The same IGES geometry was imported in Hypermesh and the autocleanup feature was used to repair the automatic detectable flaws. Other surface defects like missing surfaces, free edges, warped surfaces were repaired manually using the 'Quick Edit' feature in the geometry tab of Hypermesh. The surface cleanup was performed considering a minimum element size of 1 mm for the flange and bell regions. The barrel region cleanup was performed using a reference element size of 3 mm.

2.1.2 Meshing

2.1.2.1 Meshing differential in ANSYS

ANSYS auto mesh provides a strong algorithm to mesh the whole geometry. The cross shafts pressure loads are the highest amplitude loads in the differential and thus the mesh in cross-shaft was refined to avoid stress singularities. Also as the rotational reaction is obtained at the ring gear nodes the mesh in that region is also refined to reduce the stress concentration. The mesh quality metrics used are warpage, skew and jacobian. The hex-dominant algorithm with a combination of hex and tet elements was used to reduce the

model size further. The images below show the percentage of elements failing in these criteria. *Figure 4* shows the meshed model of the optimized differential case. Only 1% of the elements fail for a quality target of 0.5. *Figure 5* shows the mesh quality contour and *Figure 6 & Figure 7* show the mesh metric of element quality. The element quality mesh metric in ANSYS combines all the mesh quality targets like warpage, aspect ratio and jacobian.
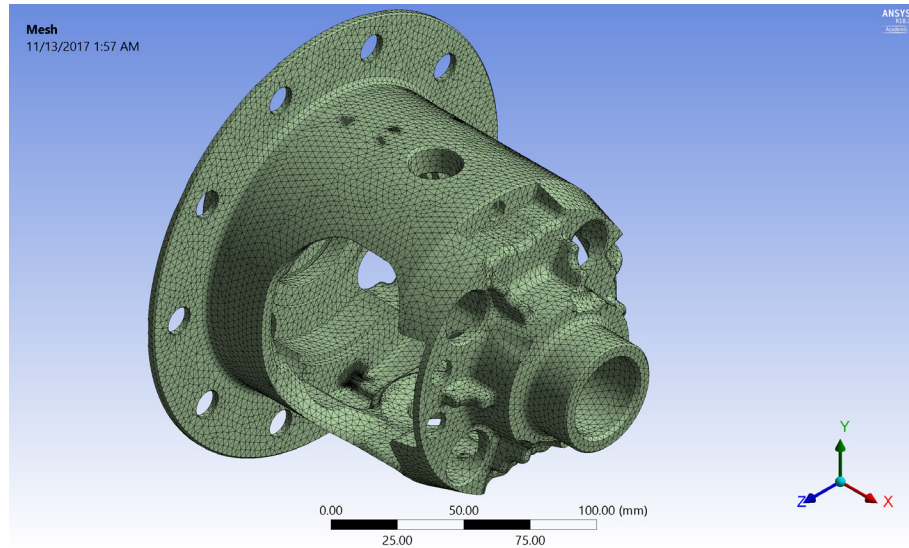
Figure 4 Ring gear and optimized differential design meshed in ANSYS
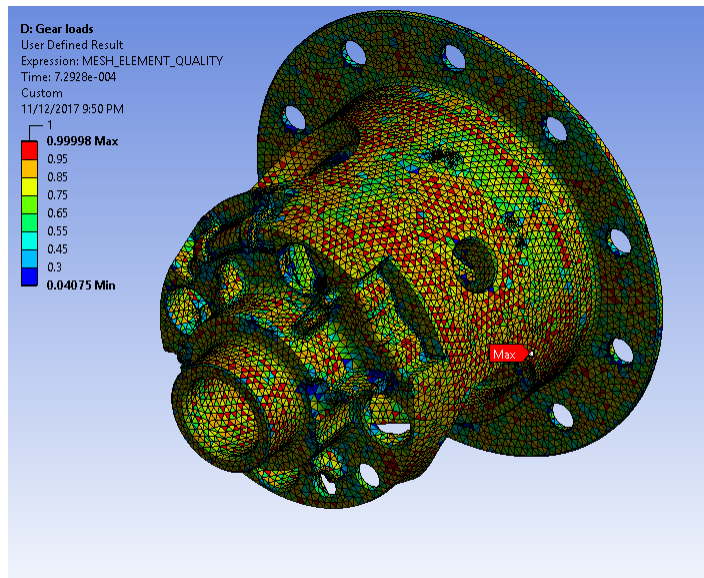
Figure 5 Mesh quality contour plot in ANSYS

17
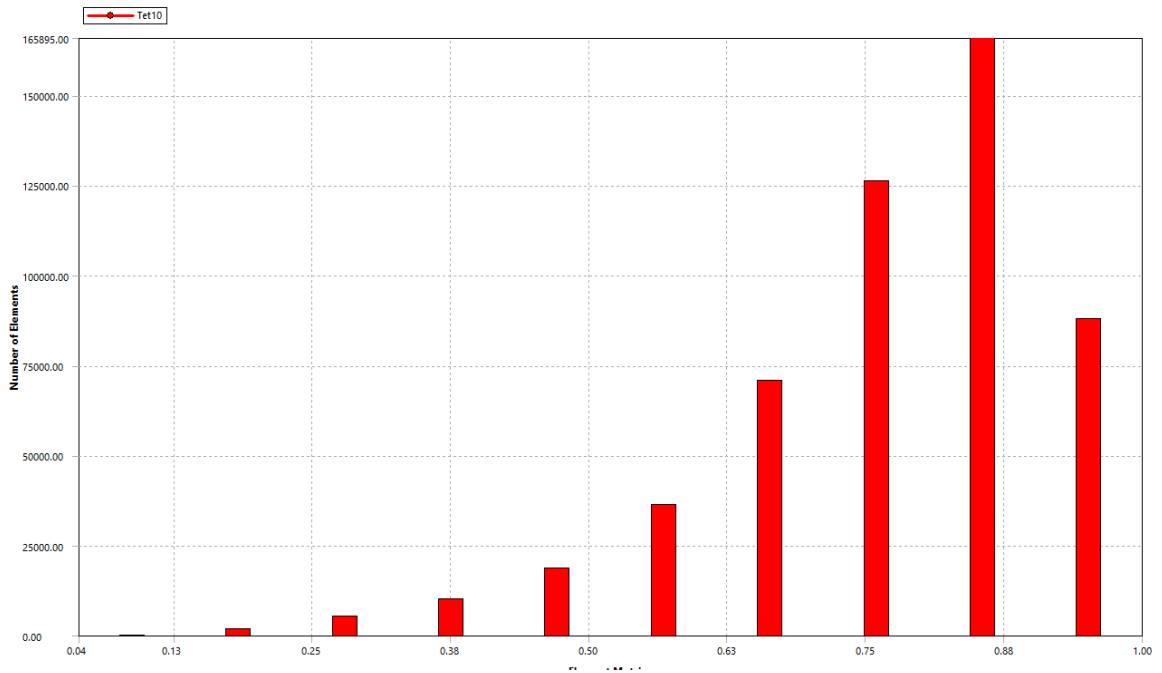
Figure 6 Mesh Metric graph from ANSYS showing quality of elements in terms of number of elements
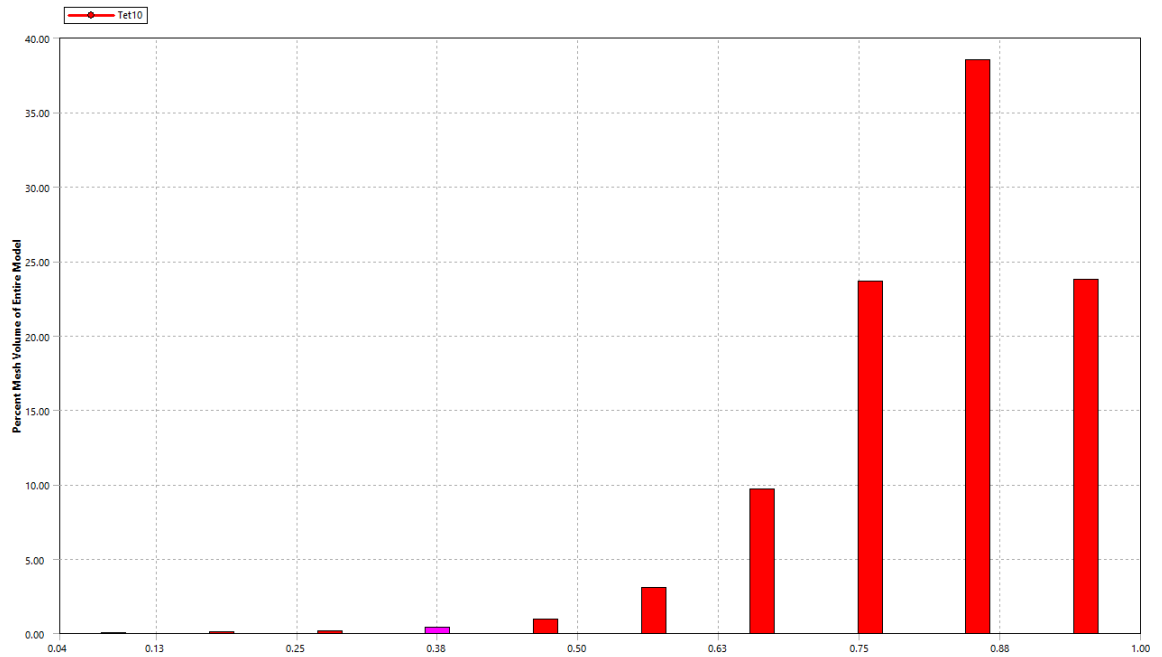
Figure 7 Mesh metric graph showing percentage of failing elements

18

2.1.2.2 Mesh validation in ANSYS

A mesh convergence study was performed in ANSYS to select the most suitable size of mesh. The constraints to be optimized in this mesh convergence study were quality of elements of created, geometry captured and solver memory available. The first mesh size selected 4 mm. The stress levels obtained with this mesh size were way higher than the ultimate stress. The maximum stress is observed in the cross-shaft region as expected. However, these values were higher than that observed in the static analysis of the differential. The *Figure 8* below shows the von-Mises stress contour plot with a mesh size of 4 mm. The maximum stress observed is 1784 MPa.
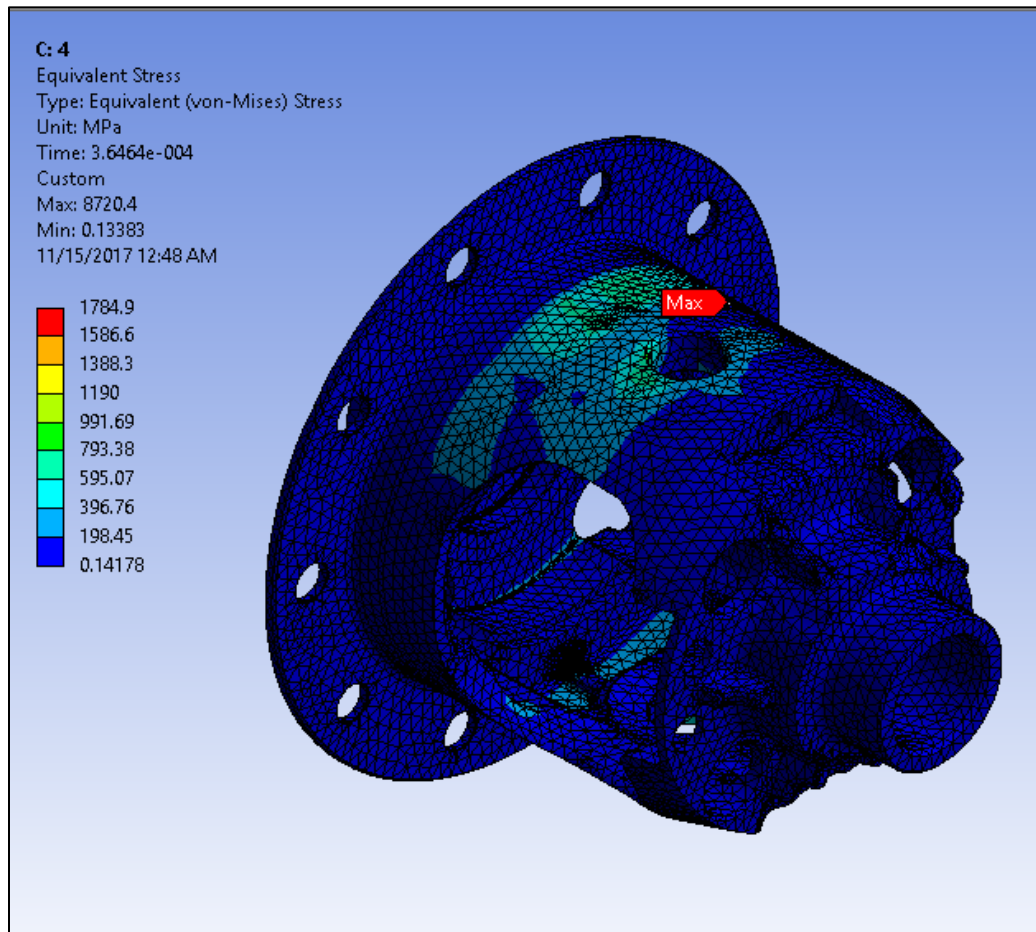
Figure 8 Equivalent(von-Mises) stress contour plot for mesh of 4 mm

19

The next mesh size selected was of 3 mm. A significant change in the maximum stress value was observed from the 4 mm mesh. *Table 1* shows the comparison of results between the 3 and 4 mm mesh sizes. A change close to 54% is observed and the values observed are close to initial simulation results.

Table 1 Maximum von-Mises stress comparison between mesh sizes of 3 and 4 mm

Mesh size (mm)	Max. von-Mises stress	% Change
4	1784.9	54.4349824
3	813.29	
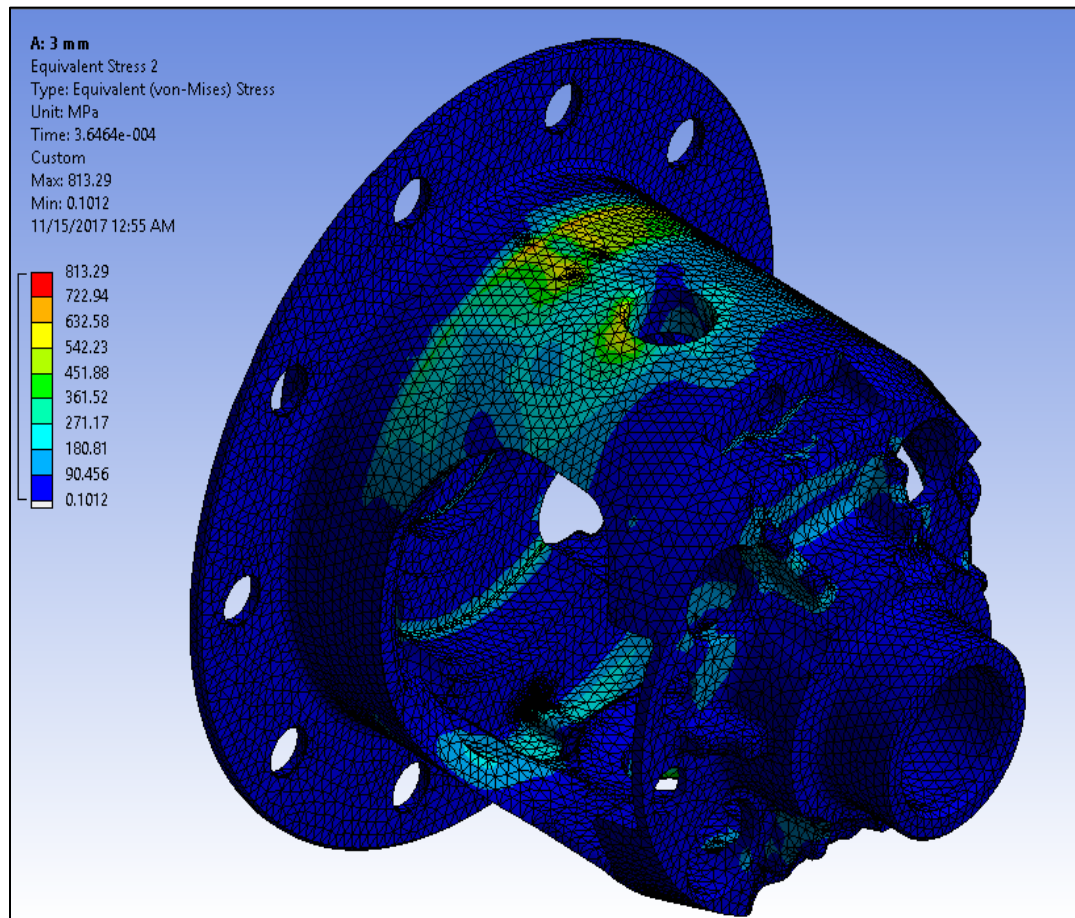
Figure 9 Equivalent von-Mises stress contour plot for a mesh size of 3 mm

The mesh was further refined to a size of 2 mm as there was a huge difference in results going from 4 mm to 3mm mesh. The observations from the results of 2 mm mesh were

20

counter-intuitive to the general perception that a finer mesh leads to better stress distribution and gives lower maximum values. However, due to some poor-quality elements created to capture the geometry and finer mesh size, large stress singularity is observed. The maximum von-Mises stress value observed is 2.2E06 MPa which is unrealistically high. The solver performance also deteriorates considerably. *Figure 10* below shows the solver performance for one substep of loading out of the total 36 loadsteps. The solver memory required is around 14 GB which is close to maximum available memory of 16 GB. The solution time is also approximately 6 times more than that of the 3 mm mesh. These differences however are not of concern if better results than the 3 mm mesh would have been observed. *Figure 11* shows the mesh contour plot for equivalent von-Mises stress with the stress singularity region observed. As we do not have much control over meshing in ANSYS and localized face meshing is not possible controlling this aspect is not possible. The work around this problem is to generate a mesh in a pre-processor tool like Hypermesh and import the mesh in ANSYS to compare the results. However, in such a case all the meshes need to be created in the same pre-processor and then the same mesh convergence study needs to be redone to get a fair comparison in results. For the current study though the auto-generated mesh from ANSYS with a mesh size of 3 mm has been used considering all the constraints like most accurate stress distribution, geometry capture, solver time and solver performance.

Details of "Solution (A6)"		Details of "Solution (D6)"	
Adaptive Mesh Refinement		**Adaptive Mesh Refinement**	
Max Refinement Loops	1.	Max Refinement Loops	1.
Refinement Depth	2.	Refinement Depth	2.
Information		**Information**	
Status	Done	Status	Done
MAPDL Elapsed Time	40 m 10 s	MAPDL Elapsed Time	3 h 47 m
MAPDL Memory Used	6.3125 GB	MAPDL Memory Used	14.869 GB
MAPDL Result File Size	1.0293 GB	MAPDL Result File Size	2.4945 GB
Post Processing		**Post Processing**	
Beam Section Results	Yes	Beam Section Results	Yes

Figure 10 ANSYS solver performance comparison between mesh sizes of 2 and 3 mm

21
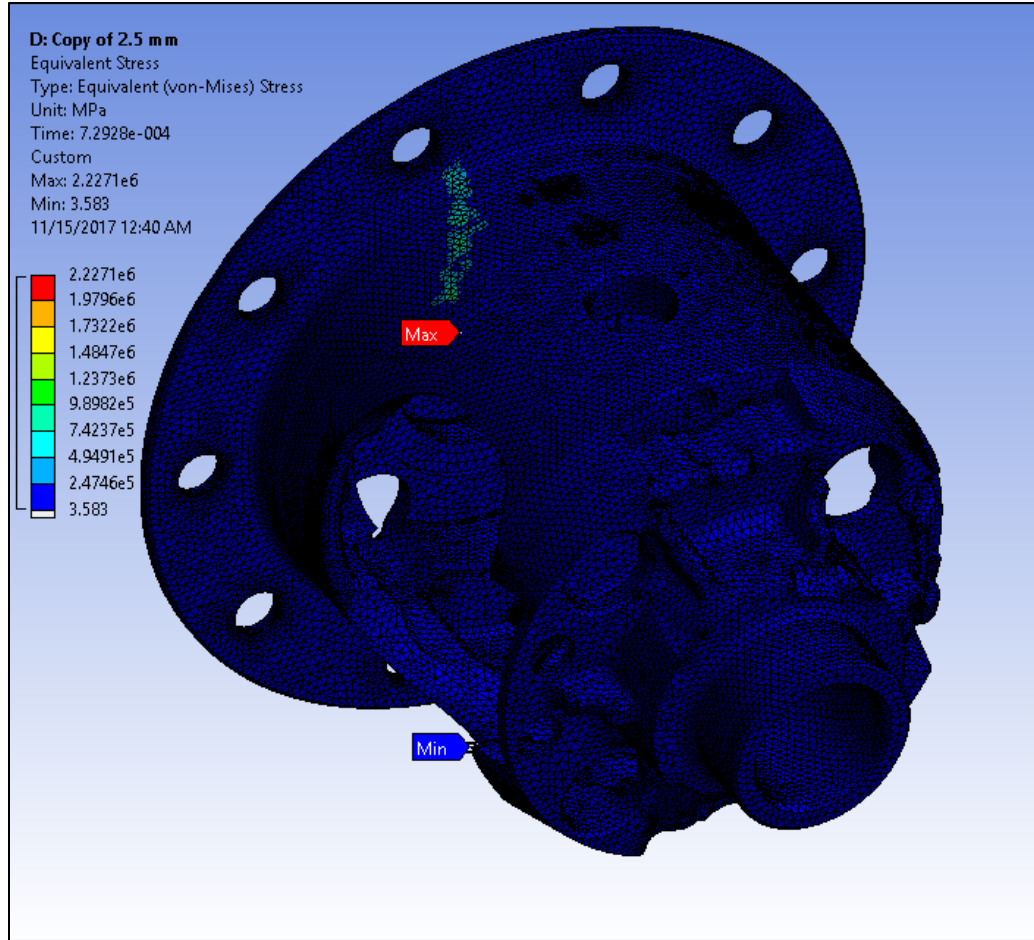
Figure 11 Equivalent von-Mises stress contour plot for a mesh size of 2 mm

2.1.2.3 Meshing differential in Hypermesh

For meshing in Hypermesh a 2D surface mesh of quads and trias was created to capture the geometry. Effort was made to use maximum quad elements to reduce the computation time of the model in Hypermesh. A 3D mesh was generated using the surface mesh and pyramid and tetrahedral elements were generated. According to Altair's Guide 0.1 is an acceptable value for tet collapse. 1 is the best quality to achieve. *Figure 12* and *Figure 13* show the meshed model of differential and ring gear respectively in Hypermesh. Much better control over meshing is possible in Hypermesh. But as time integration of results for a static simulation is not possible in Optistruct, the primary solver for this study will be ANSYS. A mesh convergence study hence is not conducted for Hypermesh. The mesh size selected is based on the mesh size used by Mr. Pankaj Kalan in his study (Kalan 2016).

22
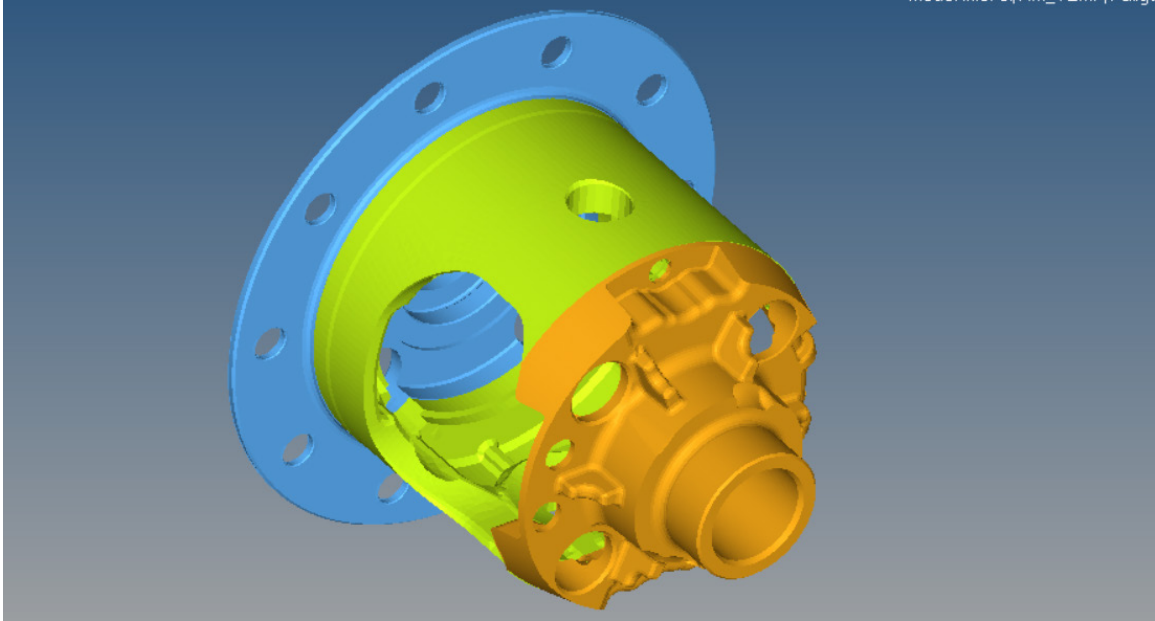
Figure 12 Meshed differential model in Hypermesh
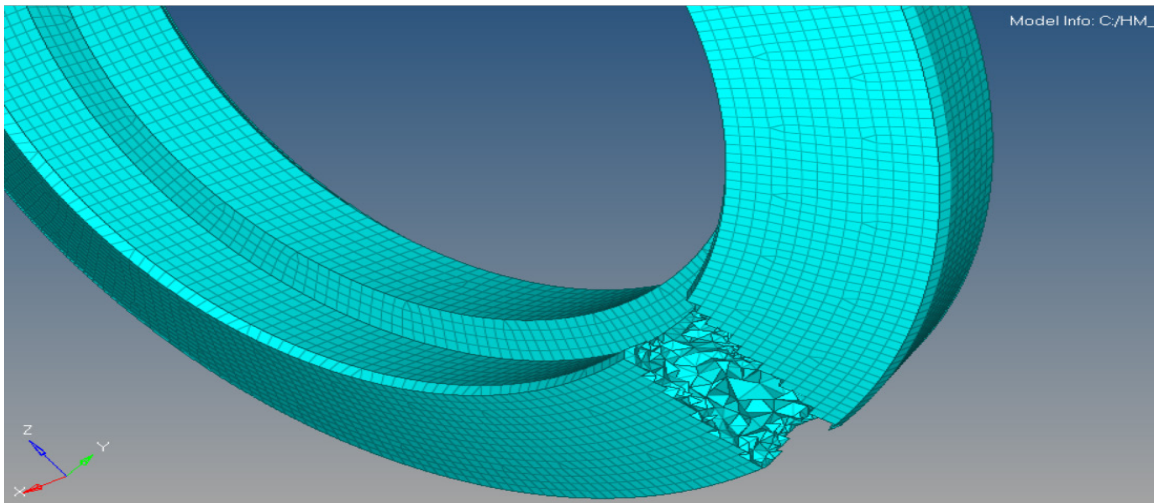
Figure 13 Meshed model of Ring gear

2.1.3 FEA analysis set-up of Differential case

2.1.3.1 Loading of the differential case

The loading location and load amplitudes details for the differential were provided by Eaton. As the loading data provided is for static analysis and time history is not available these static load cases need to be used for a time dependent analysis. The bearing pressure,

side gear separating loads, pinion gear separating pressure are treated as mean stress the component is under. The ring gear force is the time dependent load based on vehicle speed.
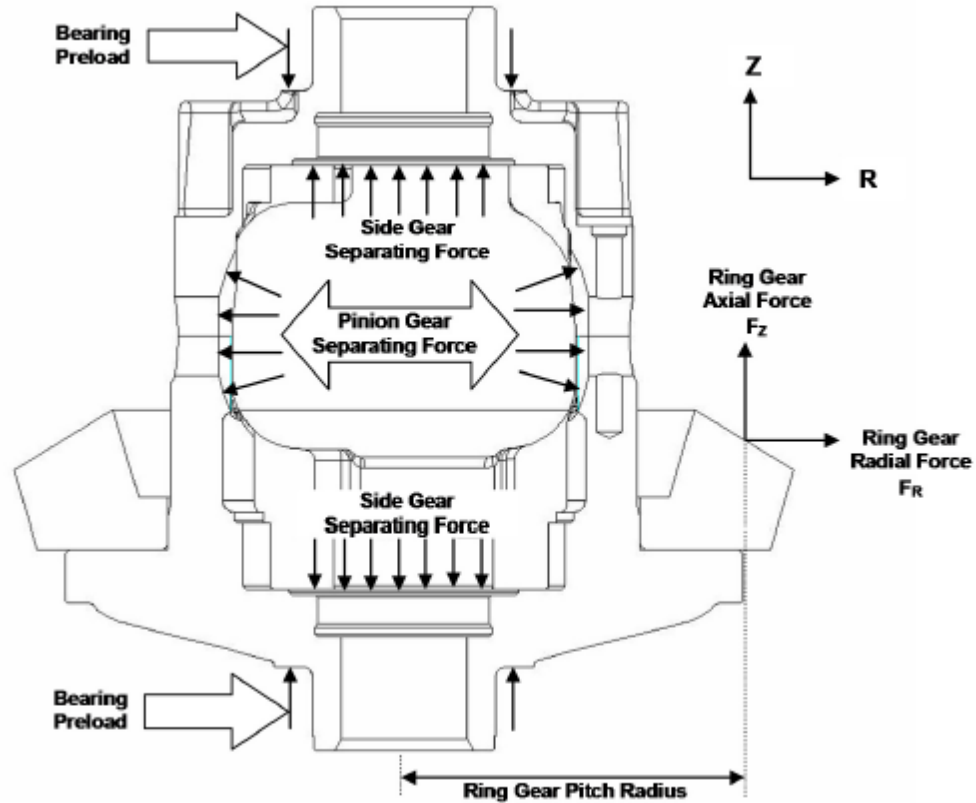
Figure 14 Static loading diagram of differential (EATON 2015)

Figure 14 shows the static loading of the differential. The ring gear force is simulated to change in a time dependent manner. The current simulations are performed for a vehicle speed of 70 mph (31.29 m/s). The angular velocity of the ring gear is calculated as 60 Hz and the ring gear engaging force is applied in intervals of 10°. So, the 36 ring gear forces need to be applied in time of 0.016878 seconds. This approach was inspired from SAE report for fatigue analysis of differential cases. (S. Sreedhar 2006). The table below gives the magnitude of load and pressure values for forward and reverse operation of the differential. *Table 2* shows the values of loads and pressures acting on the differential.

The fatigue analysis of the differential case is performed in two solvers, ANSYS and Optistruct. *Figure 15* shows the loading of differential in both the solvers. In ANSYS a static simulation is performed and the results are integrated over time for all the 36 load steps. The ring gear has three force components i.e. radial, axial, and tangential. Hence 36 cylindrical co-ordinate systems were defined at the center of the ring gear pitch circle to define the three force components. However, time integration of linear static cases is not possible in Optistruct and hence the fatigue process manager must be used. This requires defining fatigue properties like S-N curve for the material and time varying load history. To use the currently available static load-cases in a fatigue environment for Optistruct, individual step functions are required to be defined which is a tedious process. *Figure 16* and *Figure 17* show the time varying load functions defined in both the solvers.

Table 2 Magnitude of Load and Pressure values for differential

	Force Magnitude(N)	Surface Area(mm^2)		Pressure(Mpa)
Pinion Gear Force	15381.18	948.68	1	16.21
		948.68	2	16.21
Side Gear Force	26150.90	907.90	F	28.80
		2460.52	B	10.63
Bearing Preload	2224.00	875.66	F	2.54
		902.00	B	2.47
Cross Shaft Load	51883.22	187.93	1	276.08
		187.92	2	276.09
Ring Gear Radial Force FORWARD	34140.2	NA		NA
Ring Gear Axial Force FORWARD	7589.4	NA		NA
Ring Gear Radial Force REVERSE	34140.2	NA		NA
Ring Gear Axial Force REVERSE	7589.4	NA		NA
Ring Gear Tangential force	63338			

25
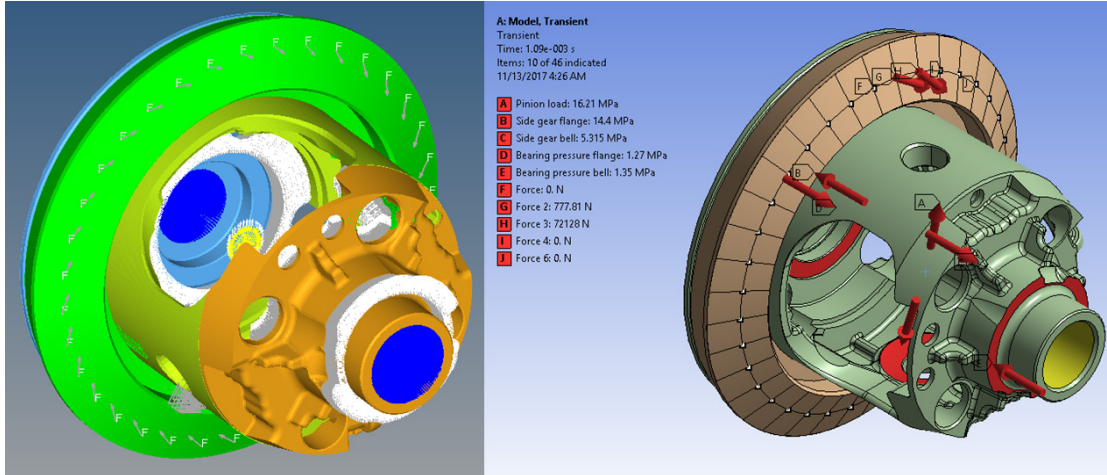
Figure 15 Loading of differential case in ANSYS and Hypermesh (Left image-Optistruct; Right image- ANSYS)
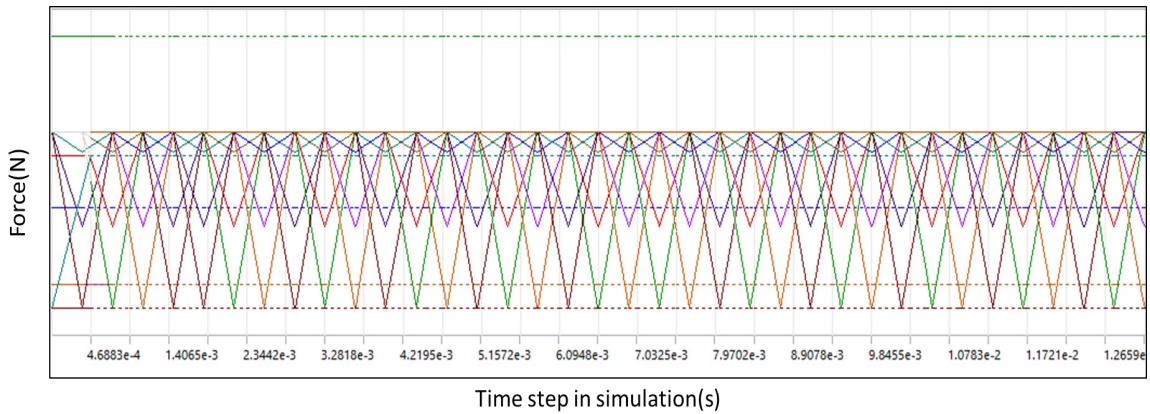
Figure 16 Time varying load steps superimposed in ANSYS Mechanical
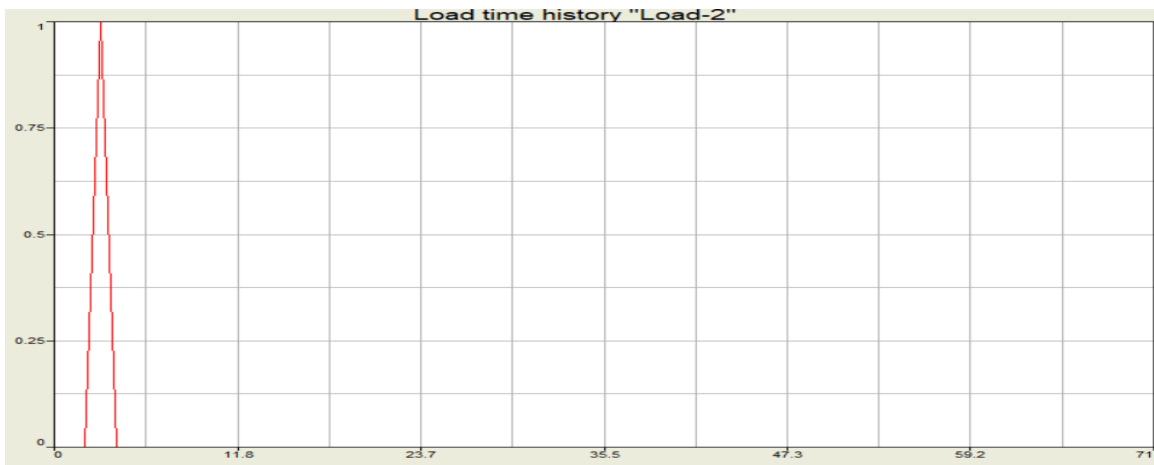
Figure 17 Step function for second ring gear load step in Optistruct

26

2.1.3.2 Boundary conditions for differential case FEA.

The boundary conditions for this simulation were provided by EATON in their reported FEA analysis for the differential case. The ring transmits rotary motion from the engine to the differential assembly. Hence the case needs to be free to rotate about the X-axis which is the axial direction of ring gear and differential case. As per the report the flange end of the differential is constrained for all DOF's other than the rotary direction. The bell end of the differential is constrained in the radial direction and is free for displacement in the axial direction to accommodate displacement due to loading of the differential. The image below shows the loading and boundary conditions for the model as provided by EATON. For fixing the rigid body motion of the differential two approaches are possible and are selected based on the FEA package used. In Optistruct the tangential force at the location of gear reactions is applied and the movement of the cross-shaft region constrained so that the cross-shaft carrying pin is not allowed to rotate. In ANSYS it is possible to apply constraints in the local nodal co-ordinate system easily and hence the tangential movement of nodes with gear reaction forces in each step are constrained. The displacement constraints are activated and deactivated based on the load step that is being simulated. The torque for rotation is applied using the pressure loads on the cross-shaft region.
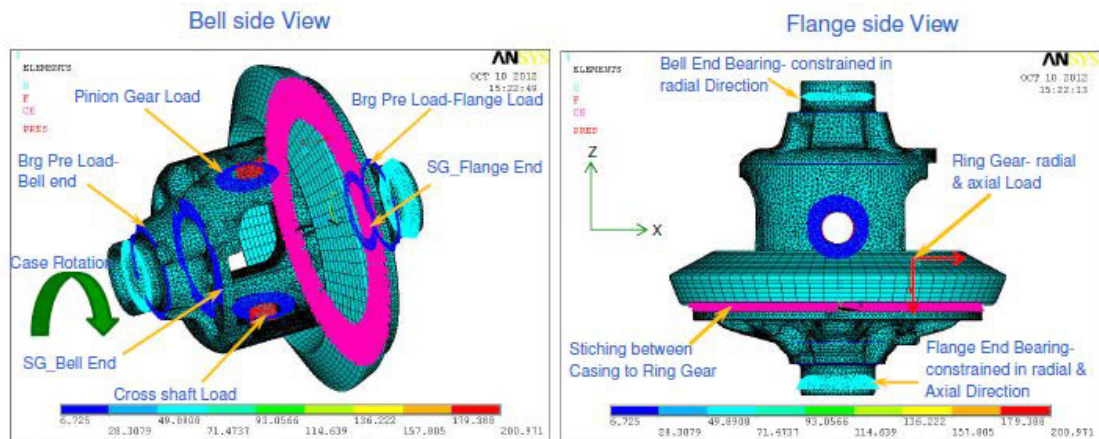
Figure 18 FEA setup used by Eaton showing loads and boundary conditions

27

2.1.3.3 Material

The simulations in earlier work for topology optimization of the differential were done using material properties provided by Eaton. However, the new chemistry LIFT alloy developed at Michigan Tech will be used to cast the new differential design. Hence fatigue simulations were carried out using the LIFT alloy as differential material and the ring material used was same as provided by Eaton. The mechanical and physical properties of both the material used is listed in the table below. These properties were used for static analysis in ANSYS Mechanical and Optistruct. The units used are consistent with units required to run a simulation in SI units in Optistruct.

Table 3 Material properties for Ring gear (Steel) and Differential case (Ductile Iron)

Property	Value
Ring Gear(Steel)	
Young's Modulus (MPa)	2.07E+05
Poisson's ratio	0.275
Density (ton/mm^3)	7.90E-09
Tensile yield strength (MPa)	370
Tensile ultimate strength (MPa)	520

Table 4 Material properties for the Differential

Property	Value
Differential (Ductile Iron)	
Young's Modulus (MPa)	1.52E+05
Poisson's ratio	0.3
Density (ton/mm^3)	7.3E-09
Tensile yield strength (MPa)	500
Tensile ultimate strength (MPa)	750

The fatigue module in Hypermesh requires to define the S-N properties before step functions for load can be defined. The material tab in the fatigue process manager has

28

several methods available to estimate the high cycle fatigue properties. The first method is estimating the S-N curve using yield and ultimate strength of the material. Optistruct has predefined constants for steel and aluminum to estimate the high cycle fatigue curve. As the ring gear is a steel and the results obtained on the ring gear are not of interest. Hence this method with more assumptions is adopted for the ring gear fatigue property estimation. For the ductile iron property estimation, the single slope intercept method was used. The user input properties are the yield and ultimate strengths, cycles considered as unlimited life, slope of the linear curve and the alternating stress axis intercept value. These values were approximated to get a curve like that found in literature. The figures below show the S-N curves for both the materials used in the model on a log-log scale. These are approximate curves and more accurate results can be obtained using the data generated in the future scope of the fatigue testing project. The reference curve used was taken from the Ductile Iron Society database ((Ductile Iron Society 2013),*Figure 19*).
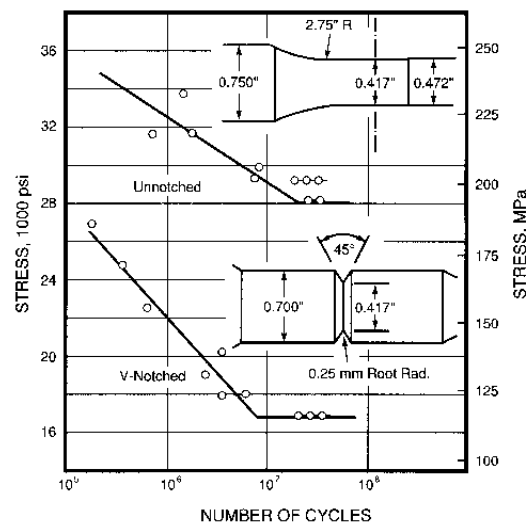
Figure 19 S-N plots of ductile iron for notched and unnotched specimens((Ductile Iron Society 2013)

29
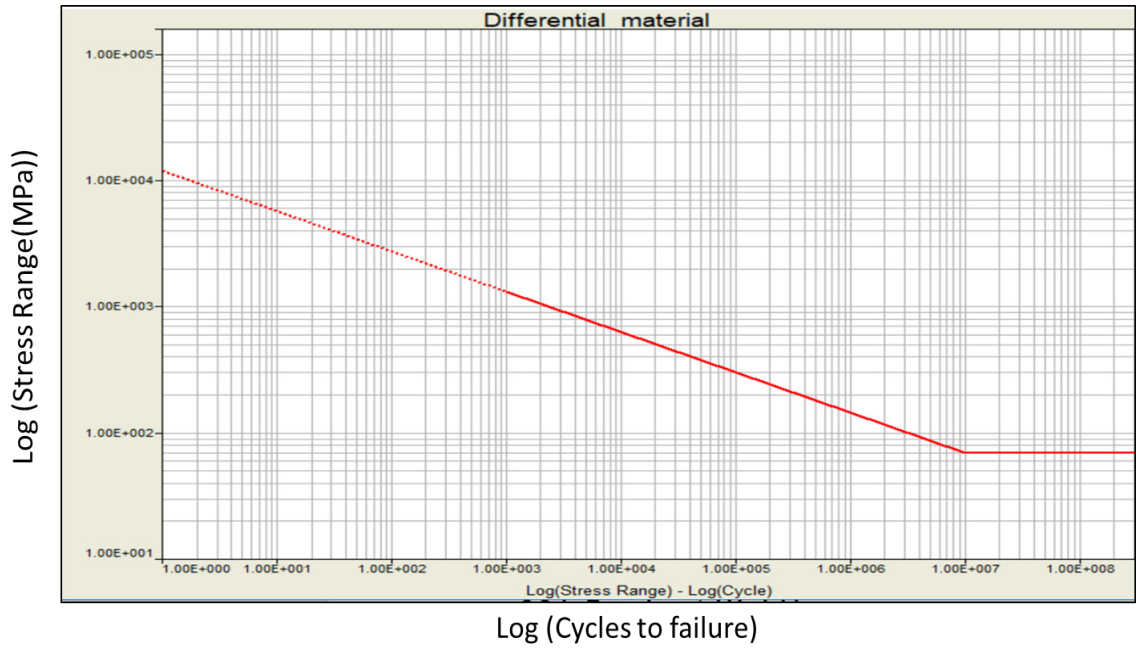
Figure 20 S-N curve for differential material (ductile iron) plotted in Hypermesh

30

3 FEA Fatigue Model and Fracture Mechanics Model

3.1 FEA Fatigue Analysis of Differential

The fatigue analysis of the differential was conducted in ANSYS workbench mechanical. As the S-N data for the materials used is not available a new approach needs to be adopted for analyzing the fatigue of the differential case. Fatigue life of a component depends on mean and alternate stress the component experiences. The pressure loads due to differential gears reaction force are considered as the stresses acting as a mean stress acting on the differential. However, fatigue stress is a time dependent phenomenon and hence a transient force is required. The ring gear transmits the rotary motion from the engine to differential case. The engagement force of the ring gear applied at increments of $10°$ around the circumference is considered as the time varying force.

Three solution strategies are possible in ANSYS mechanical for time-varying load analysis. Static analysis, transient analysis and modal based transient analysis. The criteria used to decide between a static and transient analysis generally is if the frequency of first natural mode of the component is greater than 3 times of the excitation frequency, a static analysis would represent the problem adequately. So, the first 10 modes of the differential were extracted using the block LANCZOS method. The frequency of first mode was found out to be 1400 Hz which is much greater than the excitation frequency of 60 Hz. A static approach is hence selected for the solution. However, for comparison purposes a transient simulation is also done to see difference between the two solvers.

The first solution approach is the complete static structural analysis of the differential case. The static structural solver of the ANSYS mechanical solver solves a linear equation for force and displacement as shown below.

$$[F] = [k]x \qquad\qquad Eq\ (1)$$

The solver does not consider inertia or acceleration effects in the model. Hence 36 static load cases are run in which the pressure loads remain constant in each step and the position

31

of the ring gear progresses along the circumference. This approach can be considered as a quasi-static approach that will solve each load case as independent static cases and then integrates the complete result over the time.

The second approach is a complete comprehensive transient analysis of the same problem. The loading pattern applied is similar of that of the static structural case. But the ring gear forces are applied at a frequency of 60 Hz as explained in the section 2.1.2 for loading of the differential case. The equation solved by the transient structural solver is

$$[M]\{\ddot{u}\} + [C]\{\dot{u}\} + [K]\{u\} = \{F\} \qquad Eq\ (2)$$

The major step up from static structural in this solution approach is the solver considers the effect of inertia relief and related accelerations. The variation in results if any would be discussed in the results section.

As discussed earlier the S-N data is not available and hence the Goodman diagram is used to find the critical areas for fatigue failure. The Goodman diagram has mean stress plotted on the x-axis and alternating stress on the y-axis. Hence to evaluate the mean stress values the pressure loads were applied separately on the static solver and Von-Mises stresses were extracted at each location in the model. For, alternating stresses the ring gear engagement forces are applied and the stress alterations over the time are calculated. These values are then plotted on the Goodman diagram and the locations falling in the failure zone are identified. The Goodman diagram for current analysis is shown in the Results section.

The Goodman theory which is used to identify the failure regions is mainly a uniaxial stress theory and equivalent stresses from the multiaxial stress state of the component need to be identified. Numerous methods are available to get an equivalent alternating and mean stress from the stress history. These uniaxial methods have been compared to the more popular multiaxial methods used by commercial fatigue software in the work by et al Papuga (Jan Papuga* 2102). The uniaxial fatigue theories available are signed von-Mises theory, Mason-McKnight (MMK) and modified Mason-McKnight which are compared to multiaxial theories like Dang Van and Crossland methods.

32

The study by et al Papuga concludes that in a simple proportional loading case all the methods are found to give similar accuracy for ductile materials (Jan Papuga* 2102). However, for a complex loading or a proportional loading in the presence of mean stress the modified Mason-McKnight method is found to be close to the multiaxial methods (Jan Papuga* 2102). A loading history where there is a constant non-zero load acting on the component at all times and there is at least one variable load is classified as proportional loading. This is the kind of loading present in the case of differential as well. Hence the modified MMK method is used to identify the failure regions.

The modified MMK method used the normal stress in the natural co-ordinates axes and the corresponding shear stress components to calculate the alternating and mean stress in the component. First the maxima and minima of each directional stress tensor is calculated. The maximum is recorded at the time of gear engagement and minimum is the time between the relaxation and engagement of the next step load. The formulas for the same are listed below

$$\sigma_{i,a} = \frac{max_t(\sigma_i) - min_t(\sigma_i)}{2} \qquad\qquad Eq\,(3)$$

$$\sigma_{i,m} = \frac{max_t(\sigma_i) + min_t(\sigma_i)}{2} \qquad\qquad Eq\,(4)$$

$$\tau_{ij,a} = \frac{max_t(\tau_{ij}) - min_t(\tau_{ij})}{2} \qquad\qquad Eq\,(5)$$

$$\tau_{ij,m} = \frac{max_t(\tau_{ij}) + min_t(\tau_{ij})}{2} \qquad\qquad Eq\,(6)$$

Using these calculated tensor values the alternating stress and mean stress are calculated using equations (7) and (8) as shown below. The modified MMK method uses the principal stresses to determine sign of the mean stress and is given by equation (9).

33

$$\sigma_a = \sqrt{\frac{1}{2}[(\sigma_{x,a} - \sigma_{y,a}) + (\sigma_{y,a} - \sigma_{z,a}) + (\sigma_{z,a} - \sigma_{x,a}) + 6(\tau_{xy,a} + \tau_{yz,a} + \tau_{zx,a})\}]}$$

……. Eq (7)

$$\sigma_m^* = \sqrt{\frac{1}{2}[(\sigma_{x,m} - \sigma_{y,m}) + (\sigma_{y,m} - \sigma_{z,m}) + (\sigma_{z,m} - \sigma_{x,m}) + 6(\tau_{xy,m} + \tau_{yz,m} + \tau_{zx,m})\}]}$$

……. Eq (8)

$$\sigma_m = \sigma_m^* \frac{\sigma_{1,max} + \sigma_{3,min}}{\sigma_{1,max} - \sigma_{3,min}} \qquad Eq\ (9)$$

3.2 Fatigue test design and crack propagation model

3.2.1 Experimental Variables for fatigue testing

The objective of this study is to observe the effect of casting skin generated by casting processes using inorganic sand, organic sand and machined samples after removing the casting skin from samples of both the processes. Casting skin is found to reduce the tensile and fatigue strength by 9 and 40 % respectively (S Boonmee 2016). This work on compacted graphite (CG) iron and as stated by them in ductile iron has a higher Mn content than CG iron and thus a thinner casting skin. Hence the experimental variables in this study are Si and Mn content in ductile iron, effect of organic and inorganic binders and the surface roughness of the samples. *Table 5* shows the level of Si and Mn that are to be tested. A total of 9 combinations with the allowing elements are possible A flexural fatigue test was designed to obtain S-N curves for as-cast surfaces with organic/inorganics bonded castings and machined sample of each combination of Si-Mn levels. Each combination of these levels to be tested and surface conditions give a total of 24 configurations to be tested. The casting would be manufactured at the Joyworks LLC, Ann Arbor, MI.

Table 6 shows the test plan for flexural fatigue testing with for Si at 2.5 wt. % and Mn at 0.15 wt. %. Endurance limit for any material is defined as the magnitude of repeated stress cycles for which the material would last a specified number of cycles (generally 10^6 or 10^7).

34

Table 5 Levels of Si and Mn to be tested

Constituent	Level in weight percent		
Silicon(Si)	2	2.5	3
Manganese(Mn)	1	1.5	2

Endurance ratio is defined as the ratio of endurance limit to tensile strength of the material. The Ductile Iron Society states that the endurance ratio for ductile iron lies in the range of 0.4-0.5 (Ductile Iron Society 2013). As shown in table – the tensile strength for LIFT allow is 750 MPa so the endurance limit would be around 300-375 MPa. Hence the lower limit for stress levels were set to these values. The first value of 230 MPa is tested just to check for a new endurance limit if the sample fails before 10^6 cycles in the stress range of 300-375 MPa. The yield strength of the material is used as the upper limit for the stress level as it would serve as the von-Mises failure criterion at worst case flexural loading.

The test matrix also describes the number of finger molds to be used to cast the test sample. The design of these finger molds is explained in the next section of this report. Each finger mold has three as-cast samples of 3 mm thickness and three 4 mm samples which would be machined to a thickness of 3 mm.   Each pour of every composition at Joyworks would produce 190 lbs of metal which would include 3 keel blocks of total weight of 110 lbs. The rest 80 lbs is used in casting finger mold patterns to get samples for the flexural fatigue and tensile tests to get the mechanical properties of each configuration. A finger mold with varying thickness from 2-6 mm is also casted with each heat to study the mechanical and cooling properties across the range of wall thickness.

The tests are carried out on a constant speed flexural fatigue testing machine which uses a displacement based loading method. The load range that the motor in the machine can generate is up to 40 lbs. The test matrix also shows the displacement values that the test is run on for the corresponding stress level

35

Table 6 Test matrix for first phase of testing for one alloying combination

LIFT Melt R2-5 Project - Thin Walled Ductile Iron - Skin compared to Non-Skin															
INITIAL CONDITION TEST PLAN (March 29th, 2017)															
Specimen condition				Testing with 3 - 4mm Fingers						Microscopy	Testing with Keels - Rounds				
Surface	Si (wt%)	Mn (wt%)	S_{ut} (Mpa)	Tensile Test	Flexural Fatigue Test load (MPa)	Disp. on m/c (mm)	No. of Tests @30Hz	Total samples needed	No. of Finger molds (3-4 mm)	No. of Finger molds (2-6 mm)	Tensile Tests	T-T Fatigue load (Mpa)	Fatigue Tests	Total samples needed	No. of Keel molds
As-cast (3 mm)	2.5	0.15	773	3	230	0.123	3	13	9	1	3	230	3	15	5
					310	0.165	1								
					385	0.205	1								
					425	0.227	1								
					465	0.248	3					465	3		
					500	0.267	1								
Machined (4 mm)	2.5	0.15	773	3	230	0.123	3	13				230	3		
					310	0.165	1								
					385	0.205	1								
					425	0.227	1								
					465	0.248	3								
					500	0.267	1					465	3		
Total Casting Wt (lbs)	180			63							7	110			

36

3.2.2 Finger mold design

The casting pattern for finger molds was developed from the initial vertical design from work of Alexander Reinl (Reinl 2016). The fingers in this mold ranged in thickness from 2-6 mm to study the variation of properties in the target thickness for differential case. The same design was further refined and then adopted to cast the as-cast (3 mm) and machining (4 mm) samples. Figure below shows the initial design and subsequent changes in the design. The feeder design was changed to allow faster metal during pouring. The feeder from the previous design made the molten metal splash after pouring the metal. Hence the step of height in the feeder design was removed and a large radius was introduced on all sides to facilitate proper flow. Further the height of the sprue was increased to get better filling by increasing the pressure head. Radii were introduced at the feeder-sprue and sprue-runner interface. This design was adopted to cast the samples of 3 and 4 mm with an alternate 3-4 configuration. Filters used were also updated by Mr. Russell Stein and the necessary design changes were made to incorporate those. Further Mr.Thorsten Reuter working with Hickman-Williams suggested a new filter to be used and eliminate a part of the down-sprue. The *Figure 21* below shows the design change of the finger mold from the base design to final 3-4 mm thickness design. MAGMA analysis was performed to check for proper solidification and cooling of the 3-4 mm samples. The filling and solidification of the finger molds with and without the down-sprue are compared in MAGMA. The cooling rate analysis shows values comparable to that of values in thesis by Alex Reinl.

37
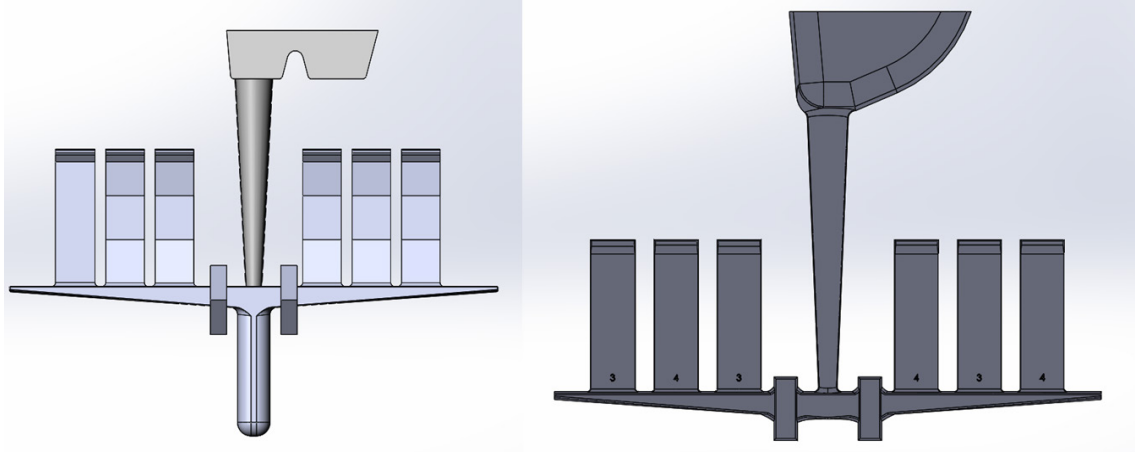
Figure 21 Finger mold base design and final 3-4 mm finger mold final design

(Left image: Base mold design with fingers of thickness 6,4,3,3.5,4 and 2 mm going L-R Right image: Final finger mold design to pour 3-4 mm fingers for flexural fatigue sample)
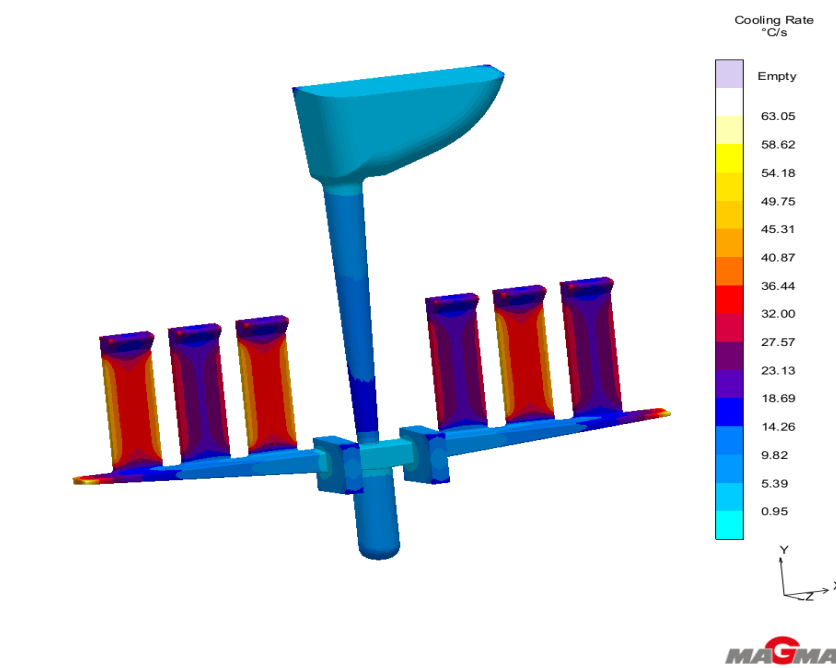
Figure 22 Cooling rate analysis in MAGMA for design with sprue well

3.2.3 Sample design

Flexural fatigue testing was selected to compare the fatigue performance of the samples due to high frequency of test machine and low cost of testing. The test consists of the

sample held as a cantilever beam and loaded by the help of an eccentric crank attached to the machine motor. The test sample is designed on the principle of a triangular beam in cantilever loading. If the length to width ratio of the beam is kept constant along the beam then the stress level remains constant along the length of the beam. This principle is explained in section discussing effect of thickness on the bending stress. Any failures occurring in this type of stress state would be due to defects in the material and surface condition.

The fatigue manual of the test machine was used as reference to design the samples. Width of the sample are constrained by the mold design and the thickness by the project test requirements. FEA analysis was performed on the sample. First a perfect triangular shape beam is simulated to see the stress contours in the beam. The geometry is then modified to accommodate it in the test machine with base for clamping in the vice and holes to attach the sample to cam shaft. The *Figure 23* shows the setup of the specimen in the flexural fatigue machine. *Figure 24* shows the 3D CAD part created for the sample.
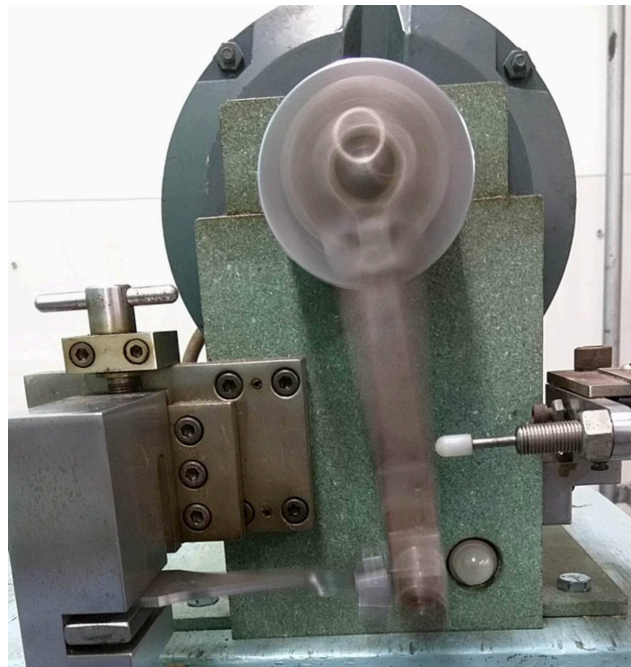
Figure 23 Specimen setup in the flexural fatigue machine
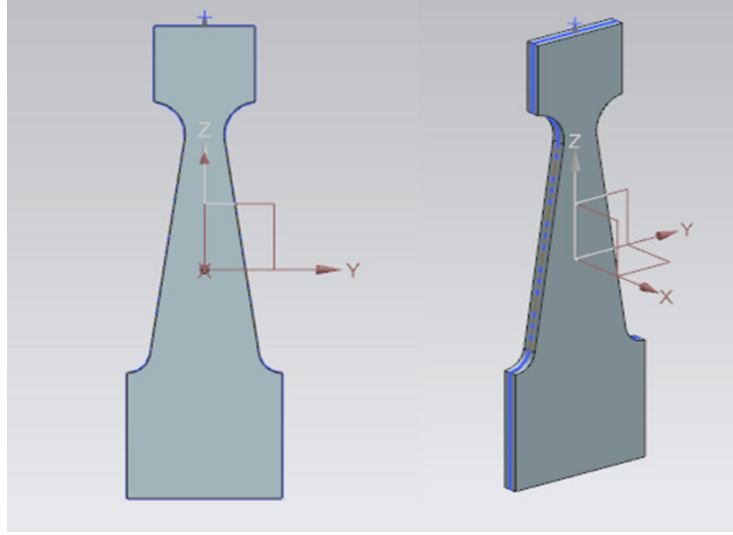
Figure 24 Flexural fatigue sample design

The width of the specimen was decided by the width of fingers in the casting mold and was set at 29.1 mm. The thickness of the specimen is also fixed at 3 mm so the only design variable available is length of the specimen. The flexural formula is used to determine the length of the specimen.

$$L = \frac{Sbd^2}{6P} \qquad Eq\ (10)$$

Considering a stress level around the endurance limit of ductile iron of 375 MPa the length of the sample is calculated as 92 mm. The loading point after attaching the sample to the cam shaft is 6.325 mm from the bolt holes. Hence 96 mm is the working length of the sample with the triangular beam as its base. Displacement values are calculated using the equation shown below for the stress levels shown in the test matrix.

$$f = \frac{SL^2}{Ed} \qquad Eq\ (11)$$

The FEA stress contour is shown in *Figure 25* and *Figure 26* below for test displacement corresponding to a load level of 37 lbf for triangular beam and the actual sample. The failure locations were analyzed after each test and sample design was updated to avoid the issues faced in each stage of test.

www.manaraa.com
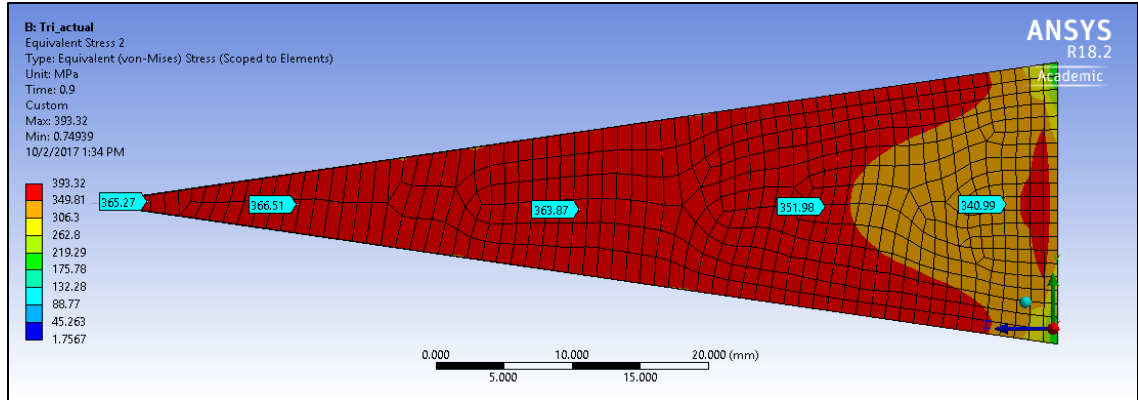
Figure 25 Actual triangular beam stress contours showing equal stress distribution

The ideal sample for this flexural test would be the triangular profile beam as shown in *Figure 25*. But to accommodate the sample in the test machine a grip section and a mount section need to be included in the design. The FEA analysis of the first sample design shows that areas of stress concentration are present at the end of the fillet after the grip section. Also, the neck region near the smaller fillet just below the clamping area is very narrow. This results in abrupt stress changes in the region. Moreover, the fillets are very sharp which pose difficulties in machining the samples properly. The stress range over the test coupon also shows a variation from 220 MPa at the narrow end gradually increasing to 327 MPa near the broader end. Most of the samples failed at the neck region near the smaller radius fillets with few exceptions which failed at the base fillet. Both not being the desired failure location.
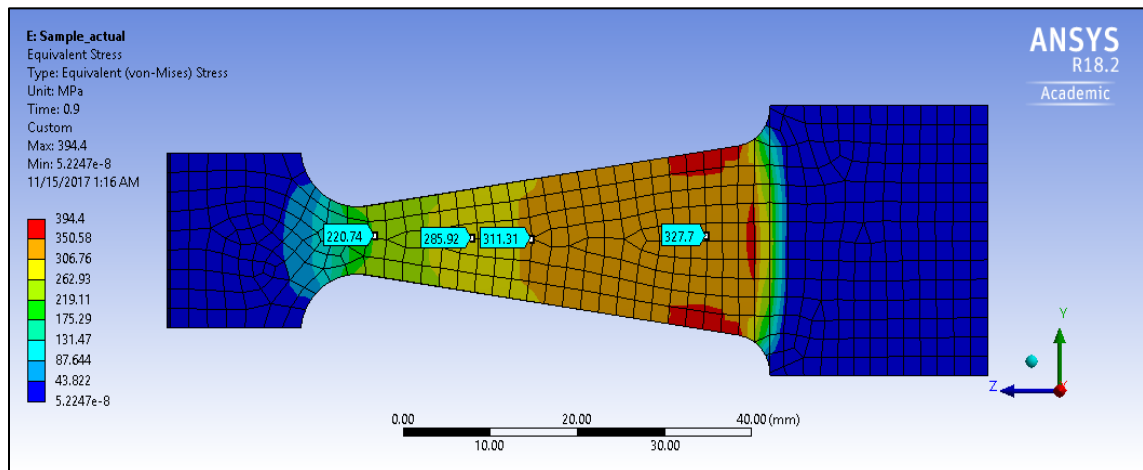
Figure 26 FEA results for stress contour plot of first sample design

41
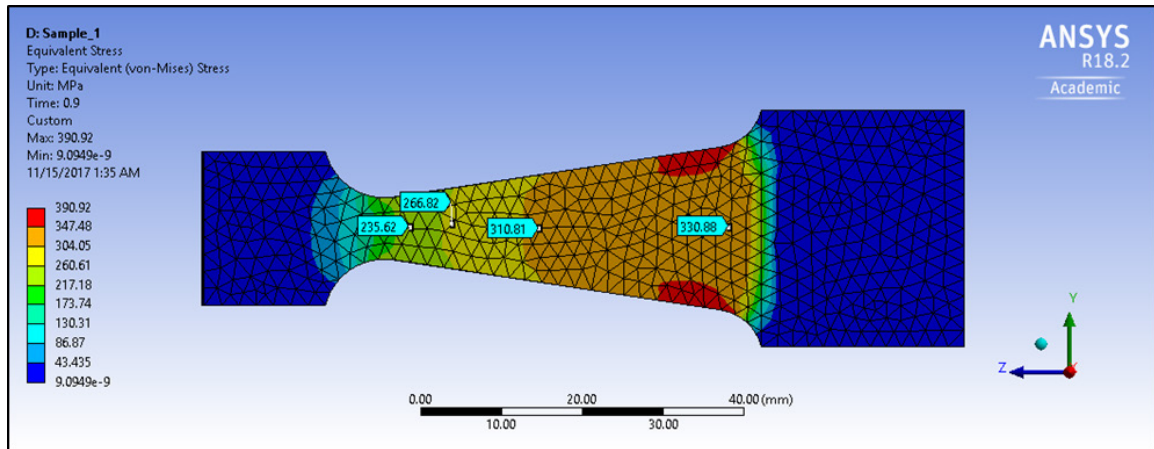
Figure 27 FEA results for stress contour plot of first iteration of sample design

Based on these observations some changes were made in the sample design. The radius of fillets on both the ends were increased to avoid problems from the first design. The radius at the clamp end of the sample was made to be half of the radius at the clamp section. *Figure 27* hows the FEA contour plot for the first iteration of the sample. The problem of stress concentrations at the end of the larger fillets was still observed in the new design. The stress range varies over the test coupon in this design too from 235 MPa at the narrow end to 330 MPa at the broad end. However, the stress contour bands seem to have smoothened out a little more in the narrow neck region than the earlier design. The test results of these samples however were like the first sample design.

Learning from these results the design was further updated. Referring some of the standard test manuals for fatigue testing it was observed that the generally used values are 6-8 times the thickness of the specimen. A more generous radius would also mean that the sample would be easy to manufacture. The length of the clamping section was also reduced slightly to help increase the length and width of the neck region near the smaller fillet. The FEA results for this iteration of the sample are shown in *Figure 28*. The problems in the first two designs have been eliminated. There is no stress concentration in the region of the larger fillet as a bigger radius has virtually merged the fillet in the edge of the sample. The most important observation being there is almost no stress gradient along the length of the test coupon with von-Mises stress values being 334 MPa at the narrow end and 336 MPa at the broader end. The maximum stress region now lies close to the middle of test coupon.

42
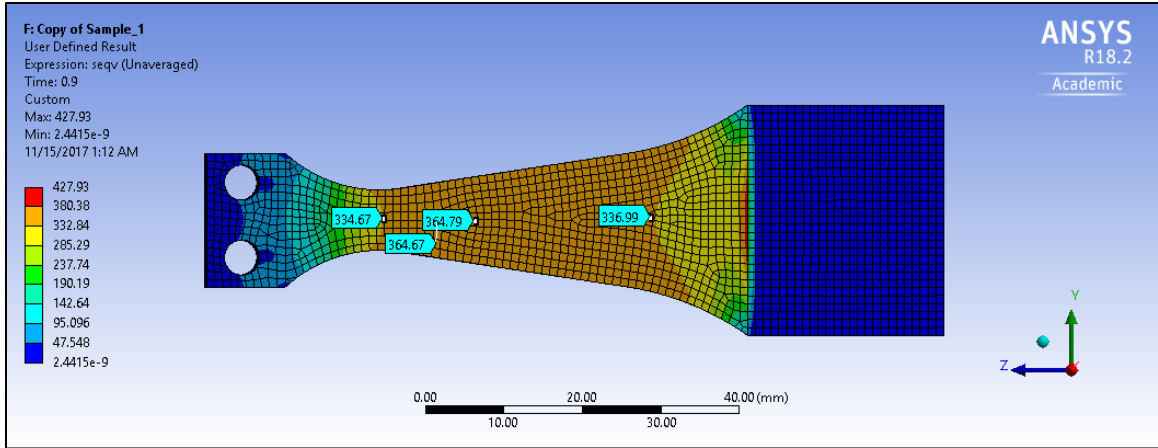
Figure 28 FEA analysis of final iteration of sample design

This design needs to be tested to verify whether the difference seen in the FEA results are translated in the physical tests as well. A better way to conduct the tests would be with strain gauges so that the FEA results can be verified and if need be the FEA analysis method can be improved. The sample drawings for all these designs are provided in App

3.2.4 Effect of thickness of test sample

The fatigue test designed is to see the effect of casting skin on thin wall ductile iron castings. A material is said to be under plane stress condition when one of the stress components acting on the material is zero. Thus, the material will experience stress only in one plane and this simplifies solving the mechanics of the problem. This stress state is generally observed in thin members experiencing loading parallel to the surface. However, the bending stress cannot be neglected. When a bending load is applied, one of the surfaces experiences tension while the opposite surface is under a compressive stress. This creates a gradient across the thickness of the specimen.

The stress in a cantilever beam is related to the bending moment at that point. The *Figure 29* below shows the representation of the test sample as a cantilever beam. The bending moment of a cantilever beam with a positive load (upward direction) is given by equation 12.

43
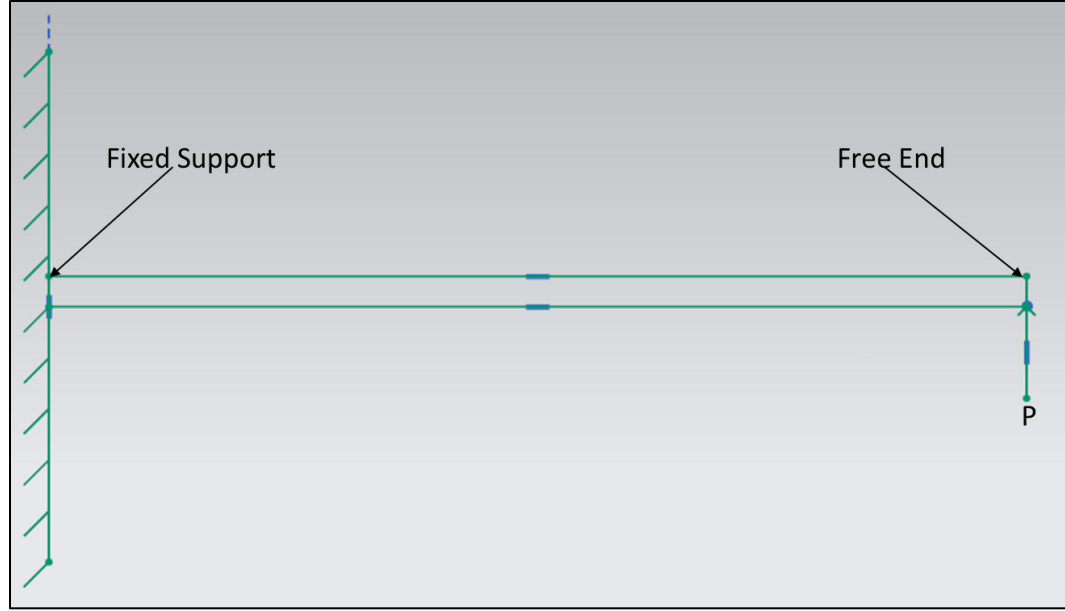
Figure 29 Schematic representation of flexural sample as a cantilever beam with a load 'P' on free end

$$M_z = P \times l \qquad\qquad Eq\ (12)$$

The thick red line in *Figure 30(a)* is the beam and the blue line shows the bending moment along the length. It can also be observed from equation 12 that bending moment only depends on the length of the beam and load applied and not on the cross-section of the beam. *Figure 30(b)* shows that area moment of inertia (I_z) also varies similar to bending moment. As the area moment of inertia (I_z) is varied linearly over the length the bending stress remains constant over the length. *Figure 30(c)* shows the plot of maximum bending stress along the length of the sample. The maximum bending stress is given by equation 13 where (d/2) is the half of thickness of the sample as maximum stress occurs on the surface. However, the stress at any point depends on the bending moment and the area moment of inertia at that point. This varies with change in location along the thickness and depends on the distance of the point from the neutral axis and is given by equation 14

$$\sigma_{b,max} = -\frac{d}{2} \times \frac{M_z}{I_z} \qquad\qquad Eq\ (13)$$

44

$$\sigma_{b,max} = -y \times \frac{M_z}{I_z} \qquad\qquad Eq\ (14)$$

(a)   (b)

(c)
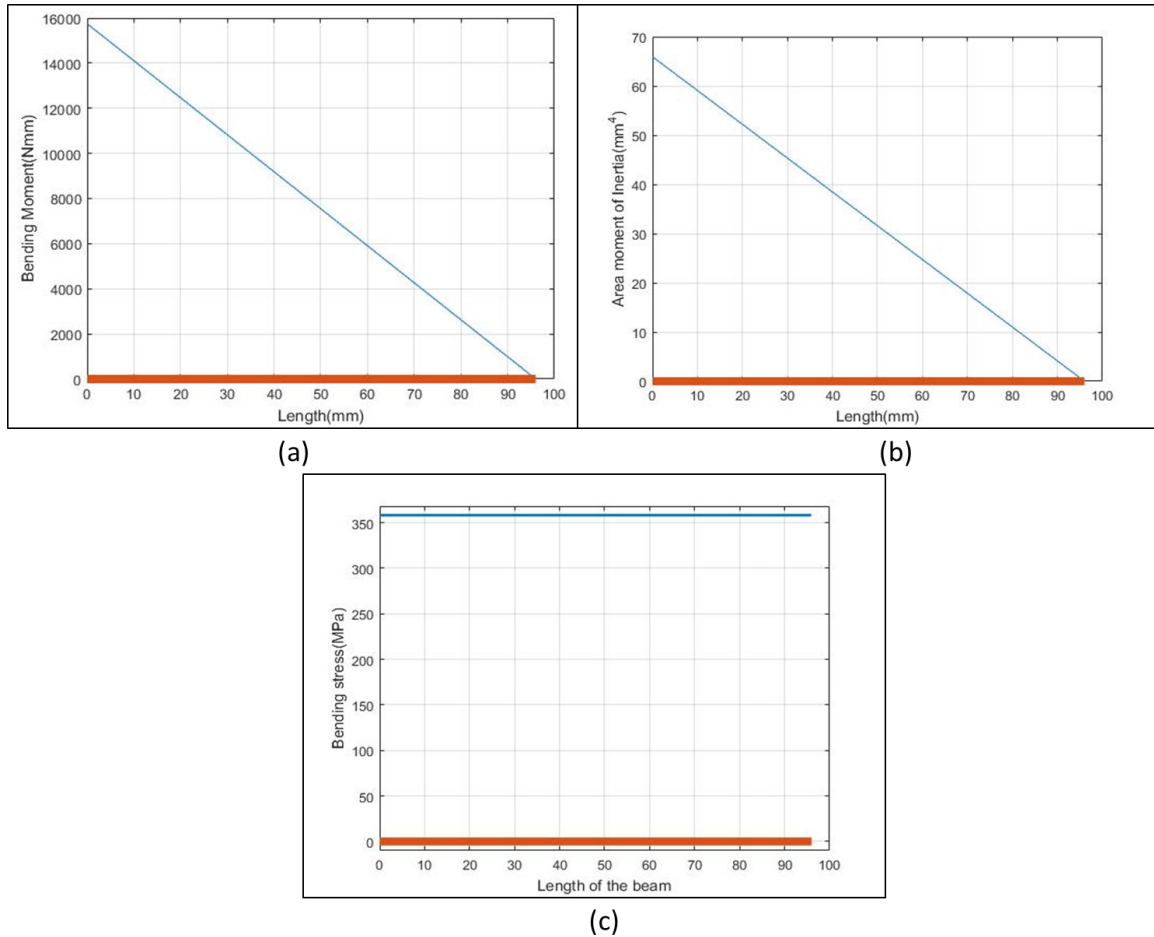
Figure 30 Plot of bending moment, area moment of inertia and bending stress on flexural fatigue sample of 3 mm thickness a) Bending moment diagram for a positive load of 37 lbf b) Change in area moment of inertia along the length of sample c) Plot showing constant bending stress along the length

But as the distance from the neutral axis (y) changes the stress across the thickness also varies with the maximum stresses occurring at the surfaces. A MATLAB code was written to observe the effect of thickness on the stresses inside the beam. As observed from the last iteration of test specimen the stress in almost constant over the length of the beam. Hence to simplify the analysis we have assumed a uniform stress over the complete length. A constant load of 37 lbf is considered and the variation of stress with change in thickness of the sample and the stress profile across the thickness is studied.

45

First, we consider the thickness of the actual designed sample thickness of 3 mm. The stress profile across the thickness is shown in *Figure 31*. The thick black lines at the top and bottom of the plot indicate the surface of the sample. The blue line is the compressive stress above the neutral axis and the red curve is the magnitude of tensile stress below the neutral axis. The maximum stress of 358 MPa is very close to the stress levels of 364 MPa in the test region obtained from the FEA analysis and hence we can say that the assumption to consider constant stress holds. We can observe that there is a huge stress gradient across the thickness of the specimen. The effect of deceasing thickness can be observed in *Figure 32*. For the same load value, a reduction of 1 mm in thickness more than doubles the stress at the surface. The maximum value of stress at the surface of the specimen is 806 MPa. This increases the gradient of stress across an even smaller thickness even further.
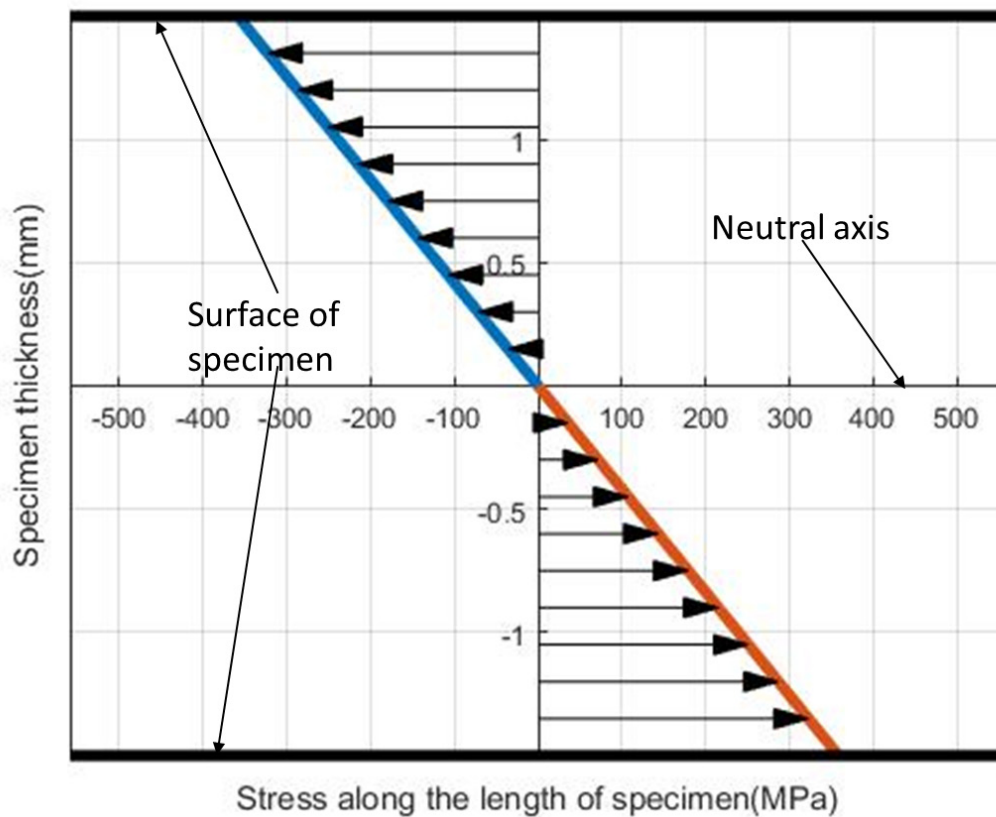
Figure 31 Stress variation along the thickness of flexural fatigue sample of 3 mm thickness

46
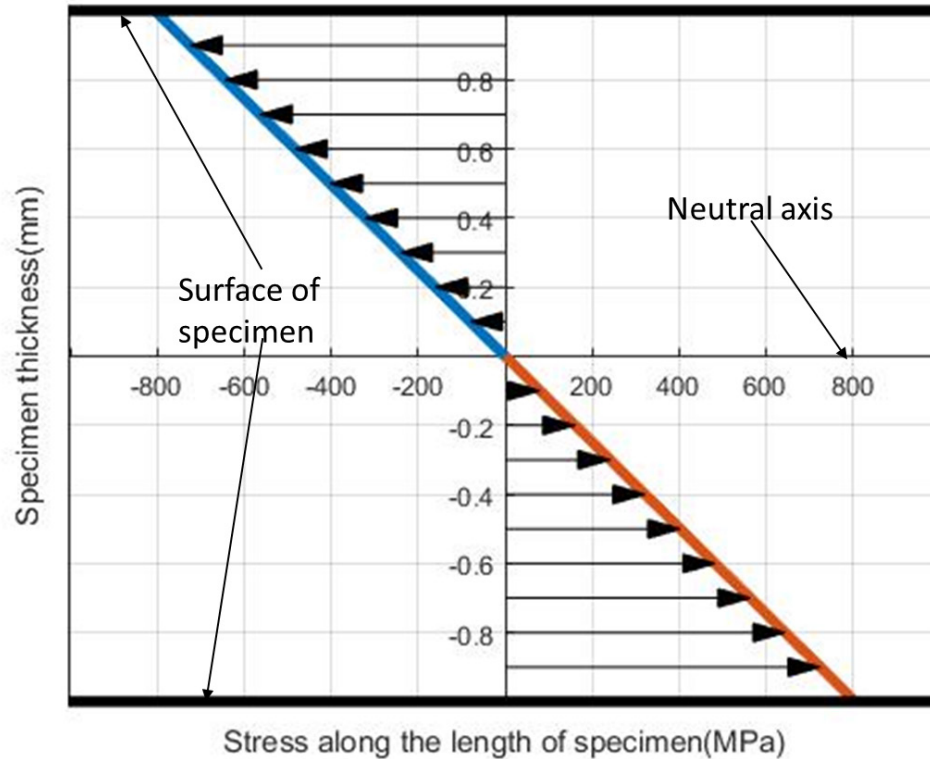
Figure 32 Stress variation along the thickness of flexural fatigue sample of 2 mm thickness

It can be said from the observations above that increasing the thickness would reduce the maximum stress experienced on the surface. Stress values for thickness from 2-10 mm have been plotted in *Figure 33*. Thus, for bending analysis of thin walled sections neither plane stress or plane strain condition can be assumed. Any FEA modeling that has to be done needs to use 3-D elements with a general strain formulation. It can be observed that the maximum bending stress drops exponentially with increase in thickness of specimen. At a thickness of 1 mm the stress gradient between the neutral axis and surface is merely 30 MPa. To determine the thickness for a beam of this length in cantilever to attain plain strain condition can be considered generally above 15 mm. The stress gradient is around 12 MPa for a beam of thickness 16 mm which can be seen in *Figure 34*. The variation in maximum stress is very sensitive to the thickness of the specimen below 5 mm. This is the thin wall region the test is being planned for. Hence, the thickness of specimen would be a critical design parameter for this study.
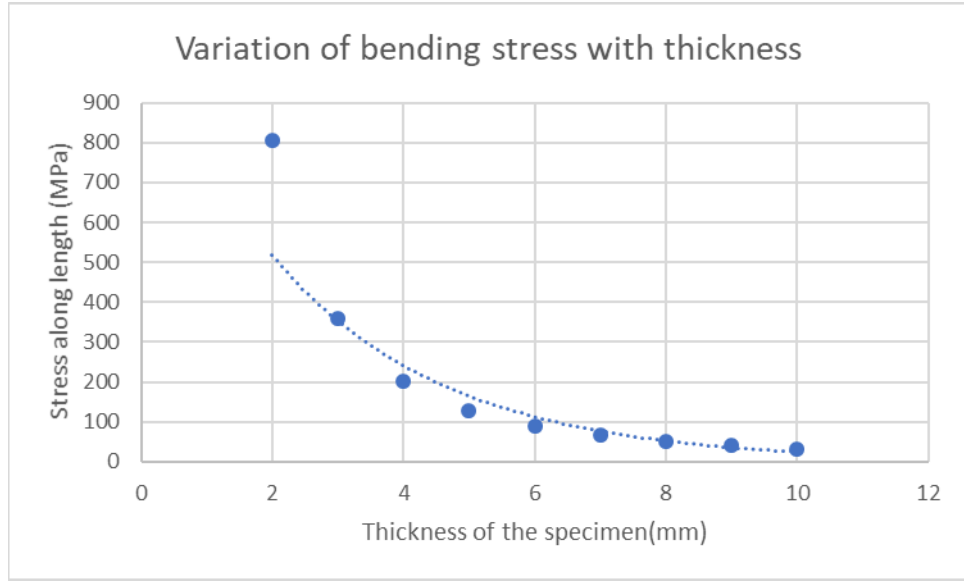
Figure 33 Variation in bending stresses on the surface of specimen with change in thickness
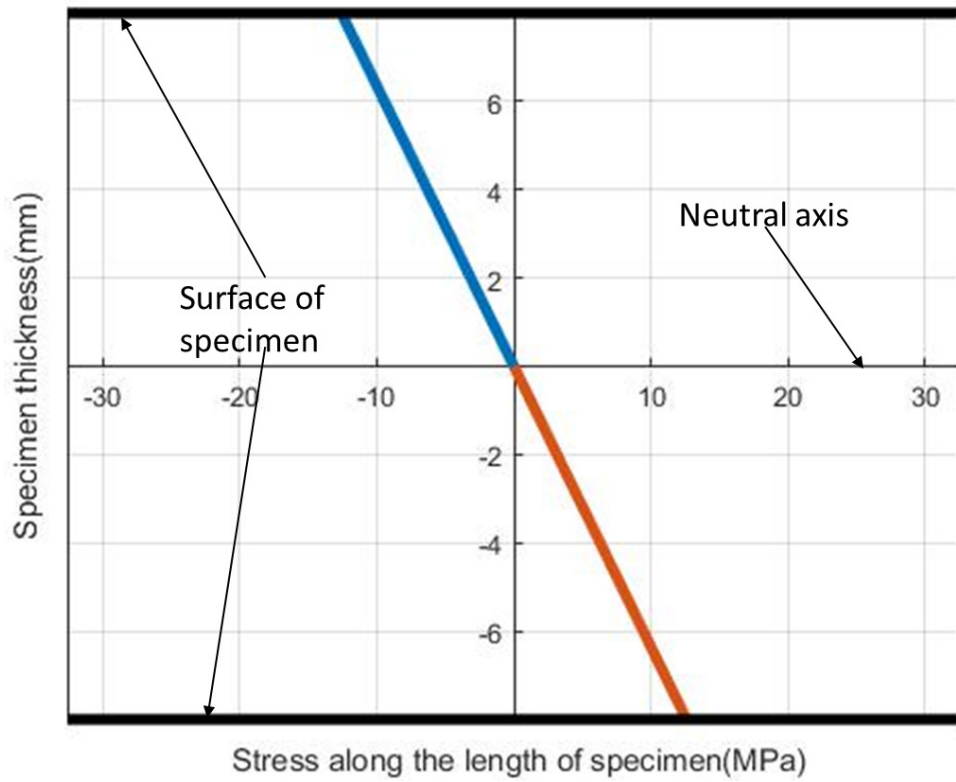
Figure 34 Stress variation along the thickness of flexural fatigue sample of 16 mm thickness

48

3.2.5 Crack propagation estimation in ductile iron

Bending fatigue generally has three stages:

1. Crack Initiation
2. Crack Propagation
3. Fracture

Crack initiation is the initial stage of crack starting in the metal matrix. The site of crack initiation is generally surface or subsurface defect in the metal. These cracks start as fine microcracks at the graphite nodule and matrix interface. The generated cracks then act as stress concentration locations and the fatigue crack then starts growing with applied stress and the second stage of propagation begins. Crack propagation further is characterized by two phases of crack growth. The first phase is the crack penetrating deeper in the material. This results in the formation of shear slip bands at the crack initiation location. In phase two the crack grows in direction normal to the direction of tensile load. The crack final grows the material and the stress concentration value reaches the toughness value of the material. The third stage of fatigue crack growth is fracture of the specimen when the crack grows through the thickness or width of the specimen.

In the case of cantilever bending of a thin specimen under completely reversed loading, each of the surface layer undergo alternate tension and compression cycles. Thus, an initial crack on the surface undergoes a crack propagation. Also in a fracture mechanics approach for crack growth, a surface elliptical crack around the graphite nodule, and a tensile load on the surface layer works in mode I of crack growth. A fracture mechanics approach coupled with some surface and metallography work can be applied to calculate the number of alternating stress cycles the material would undergo before failure. However, this method is limited to gauging only the propagation life of the sample and the crack is considered to reach a critical size defect based on the size of nodules and hence the initiation life is not considered in this model.

Crack initiation in austempered ductile iron was for low cycle fatigue behavior of ductile iron at a high strain. Crack initiation was observed within 6% of the fatigue life and these microcracks originated near the graphite nodules. The cracks originated perpendicular to the loading axis and major cracks were formed by fusion of numerous microcracks. Casting skin of 50-390 microns was observed in CGI castings of 7-15 mm thickness. (S. Boonmee 2010) . And the graphite nodules for crack initiation were observed within a surface depth of 20 microns. Hence the assumption that fatigue cracks originate in graphite nodules part of the casting skin is made.

However, little research is available on high cycle fatigue crack initiation in ductile irons. One approach considers the graphite nodules as holes and stress raisers in the matrix and the initiation life is based upon the distance of the material defects from the surface. Some of these approaches can be evaluated and applied if the test results show that the crack initiation is the major contributing factor in high cycle fatigue of ductile iron. For the current approach proposed the graphite nodules are considered as defects, as proposed by Endo in his work. (Endo 1989). In his work Endo compared the fatigue strengths of nodular cast iron with nodules and electropolished samples without nodules, and concluded that fatigue limit is controlled by the projected area of largest graphite nodule on to the surface.

Also studying literature, we can get a sense that microstructural properties have a great influence on the propagation behavior of cracks. As explained in the sample design section, if a constant stress profile is achieved along the length of the specimen the difference in fatigue life due to various design variables would only be due to the surface and microstructural defects. The most probable crack nucleation sites in a casted component would be casting defects like porosities, micro shrinkages and microstructural elements like nodules. Various models have been proposed in literature to model the crack initiation and growth rates for each of these defects.

It has been observed that location of the casting defect plays a critical role in the fatigue life of a component. A surface defect $1/10^{th}$ of the size of an internal defect present in the core of the material has the same fatigue life (Y.Nadota 2001). Hence the casting skin of

the thin walled ductile iron needs to be studied to identify the defects present on the surface of the samples. The largest or most predominant defect needs to be considered as the crack nucleation site for that sample. Shrinkage defects created during solidification can sometimes be sizeable defects and crack nucleation sites. The defect created contains discontinuous dendrites and eutectic debris which combine to form a pore on the surface of the casting (Zhao 2016). In their work Zhao et all observed that the nature of cracks originating from a shrinkage porosity is random and fatigue cracks propagate in different directions with disorderly slip bands. The study proposes a crack propagation model which can adequately represent the fatigue crack growth behavior from porosity.

The effect of micro-shrinkages on the fatigue properties of ductile iron has been studied by Paul Kainzinger et al. Contradictory results were observed for fatigue performance of the same material as conventional fatigue tests showed better fatigue performance of iron with fine micro-structure whereas crack growth experiments showed better performance of coarse microstructure iron (Paul Kainzinger 2004). The authors consider the presence of micro-shrinkages as the reason for this disparity. A fracture mechanics model has been discussed and it is observed that square root of area of defect leads to good results in estimating crack growth from micro-shrinkages (Paul Kainzinger 2004). Many other models are available in literature to model the effect of these defects in ductile iron.

The ultimate goal however in material development would be elimination of these casting defects from the component and achieve crack initiation at microstructure elements like nodules on the surface. In this study, an approach is proposed to use a fracture mechanics model on the inclusion created by defects near graphite nodules on the surface of casting. Graphite nodules act as stress concentration voids and locations of crack initiation as soon as debonding occurs (M. Dong 1993).

 In his work Dong has observed two modes of crack propagation in ductile iron.

1. Graphite nodule decohesion
2. Internal cracking of graphite nodules

The first type of behavior crack propagation starts from near spherical graphite nodules with decohesion from the matrix. The direction of crack propagation is perpendicular to the tensile loading. The second type of behavior was observed by Dong in degenerated nodules which were sites of origination of internal cracks. (M. Dong 1993)
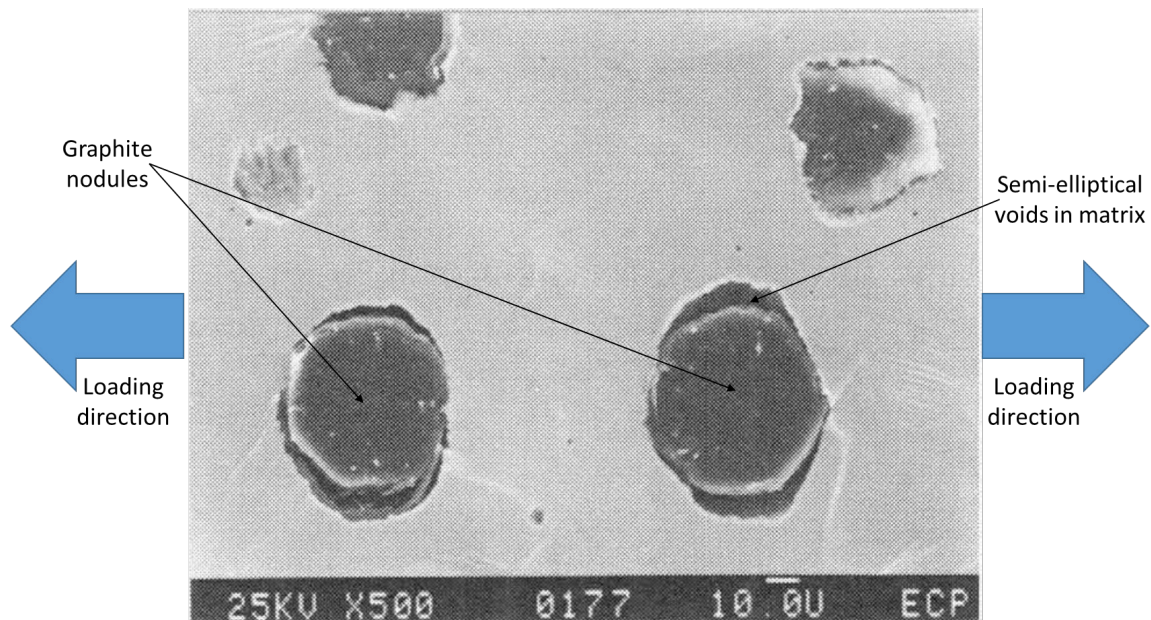
Figure 35 Nodule and matrix de-bonding with void creation (Annotation added)
(M. Dong 1993)

Fatigue performance of a component is also observed to be dependent on the surface profile and surface properties. Each type of machining process is characterized by a distinct surface profile and surface roughness. The surface roughness plays a major role in deciding the fatigue life of the component. There is a lot of literature available which studies the effect of surface parameters on the fatigue life of various metals. A method to estimate the surface stress concentration using the surface profile of a specimen is proposed by SK As and team in their work for fatigue life prediction. (S.K. A ° sa 2005) The method has been used by M. Suraratchai and group to study the influence of surface parameters on aluminum alloy. (M.Suraratchai 2008)

Taking inspiration from these works an approach to combine the stress concentration from surface profiles and the sub-surface microstructural nodules in ductile iron. The test deign

was done so that using a triangular beam in cantilever configuration would give a constant stress profile along the length of the specimen. This would facilitate that a 2D surface profile measurement can be used to represent the length of the sample to calculate the stress concentration using FEA. The stress concentration factor (K_t) is calculated using the ratio of surface and core stresses in the present study (M.Suraratchai 2008). However, as we have observed in Section 3.2.4 the stresses vary quite a lot along the thickness of a thin-walled sample. This approach would give a wrong indication of the stress concentrations at the surface. The stress concentration factor for this study has been considered as the ratio of Surface stress in a beam with measured surface profile to the Surface stresses in an identical beam with perfectly flat surface.

3.2.5.1 Surface profile measurements

The surface profile of the sample along its length is measured using a profilometer. The instrument is used to measure the peaks and valleys on the surface and give the co-ordinate of these points in microns along the length. The raw data has a vast variation between two measurements and hence the data needs to be smoothed out to reduce abrupt stress changes. A smoothing function is thus applied in MATLAB to average out the data and provide a smooth profile and avoid stress singularities in the geometry. A 51-point running averaging algorithm is used to smooth the data to eliminate the small and sharp surface troughs. The figure below shows the comparison of smoothed and raw profiles of as-cast and machined surfaces.
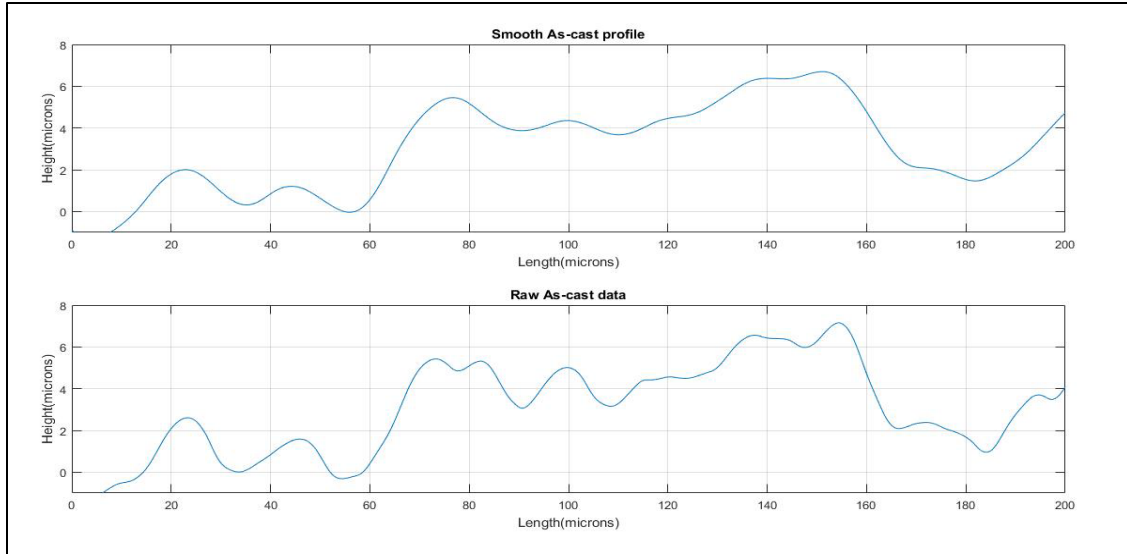
Figure 36 As-cast profile comparison of raw data and smoothed data
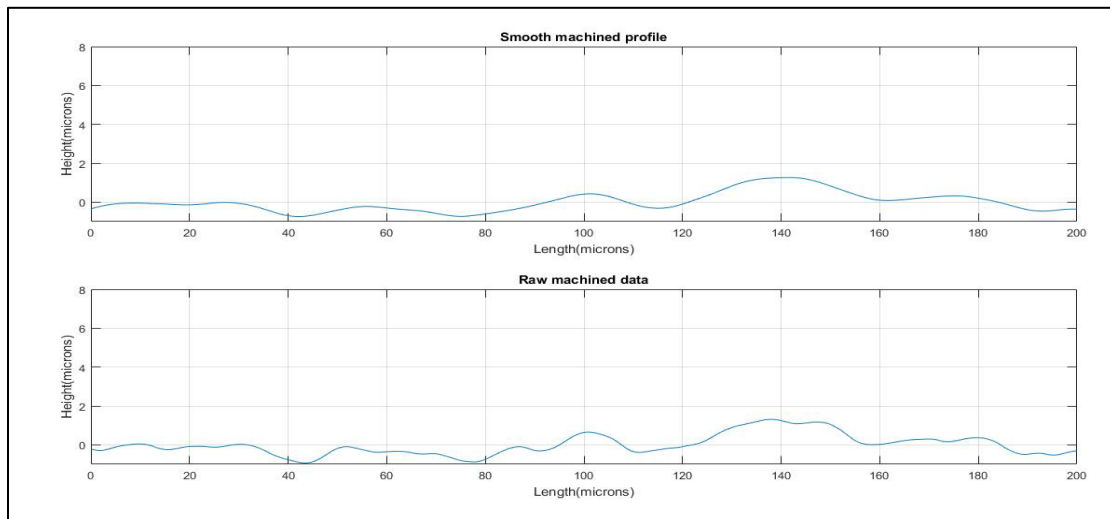
Figure 37 Machined sample comparison of raw and smoothed profile data.

As we can see the two profiles are not very different with the maximum height being 7 microns for the as-cast surface and less than 2 microns for the machined profile. However, this is just a representative calculation and does not reflect the complete length profile. The co-ordinate values from the MATLAB smoothing are then imported in UG NX10 to create a cross-sectional 2D surface representation of the length of the sample. This surface is simulated in ANSYS as a cantilever beam to calculate the k_t. Figure below shows a sample stress contour of an as-cast and a flat surface.

54
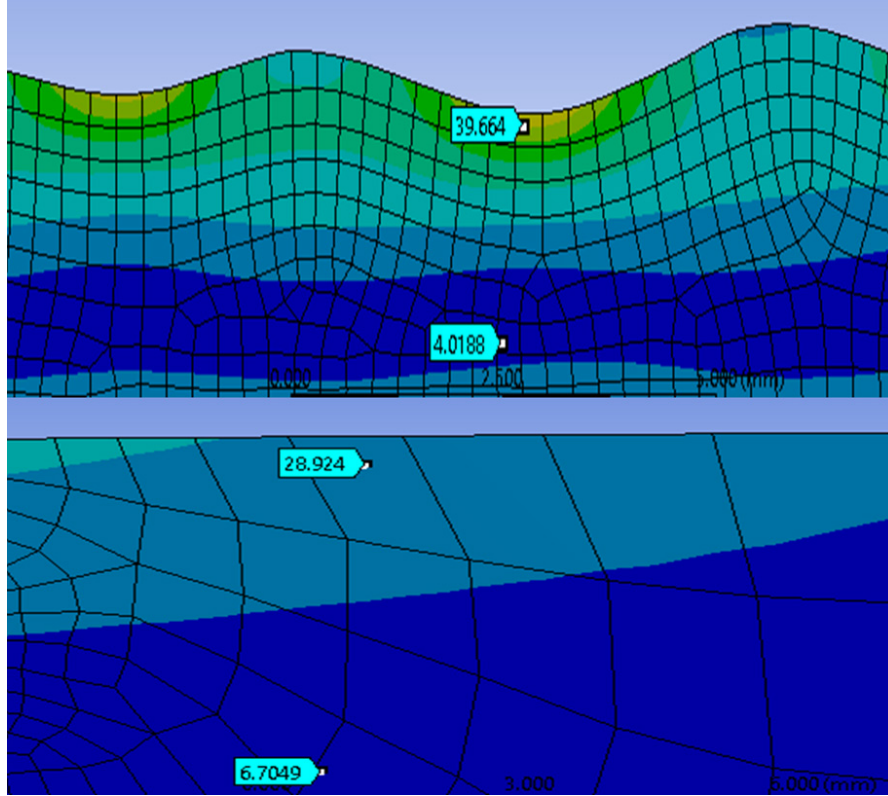
F*igure 38 Representative FEA analysis to calculate stress concentration factor for measured and flat profile*

The value of K_t is given by the ratio of stress values at the surface and the nominal stress levels in the core material

$$K_t = \frac{Stress \ on \ the \ surface \ of \ actual \ sample}{Stress \ on \ the \ surface \ of \ perfectly \ flat \ sample} \qquad Eq \ (15)$$

3.2.5.2 Fracture Mechanics approach for crack propagation

After calculating the stress intensity factor using profile measurements and FEA analysis. Paris law can be applied to get the crack propagation using the calculated value. Paris law is used to evaluate the crack growth in sub-critical regime using the stress intensity factor variation. The Paris law is given by the following equation.

$$\frac{da}{dn} = C\Delta K^m \qquad Eq \ 16$$

55

Where a is the crack length and $\frac{da}{dn}$ is the crack growth rate per cycle. C and m are material constants obtained by fracture testing of the material. ΔK is the stress intensity factor range with varying stress range.

As discussed earlier the failure mode assumed is the decohesion of graphite nodules from the matrix. This results in the formation of a semi-elliptical crack at the location of decohesion. The equation is for stress intensity factor is given below
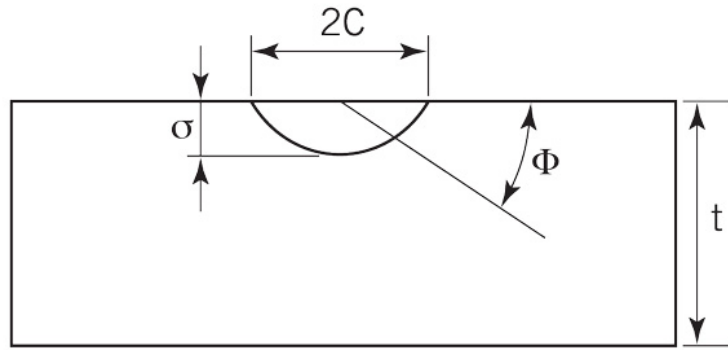
Figure 39 Semi-elliptical surface crack (Yue Cui Hui-qing Lan 2014)

$$K = \sigma Y \sqrt{\pi a} \qquad\qquad Eq\ (17)$$

Now for a semi-elliptical crack the shape factor is given by the shape factor depends upon the width, thickness of sample, loading direction and initial crack size. (J. C. Newman Jr. 1981)

$$K_{I\emptyset} = f(a, c, \emptyset. W, t)\sigma\sqrt{\pi a} \qquad\qquad Eq\ (18)$$

The detailed expression for the shape function f can be found in the work by Newman and Raju (J. C. Newman Jr. 1981). It is considered that the *'a'* is the crack length along the width of the sample and *'c'* is the crack length in depth of the sample. As the crack propagation direction is perpendicular to the direction of tensile loading, the Paris law equation become as follows.

$$\frac{da}{dn} = C\Delta K_{90°}^m \quad \& \quad \frac{dc}{dn} = C(K_t\Delta K_{0°})^m \qquad\qquad Eq\ (19)$$

56

The value for *C* and *m* are material constants and their value can be found in the literature. For the alloy considered these values are taken as *C=9.59e-14 m/cycle* and *m=4.9 MPa.m$^{1/2}$* from the literature (Matteo Benedetti 2017). Another parameter to be given as an input is the initial defect size i.e. the size of the nodules considered as defects. The approach to this would be to find the critical nodule size after testing a few specimens and use that as a guideline for initial crack size. As those results are not available, references from the literature are taken to consider the critical size of nodules. The highest number of large nodules in a 3-mm hypereutectic plate lies in the in the range of 12-17 microns and the average large nodule count is between 2000-3000/mm^3 (Pedersen and Tiedje 2008). The figure below shows the nodule size and nodule count distribution based on nodule size and plate thickness.
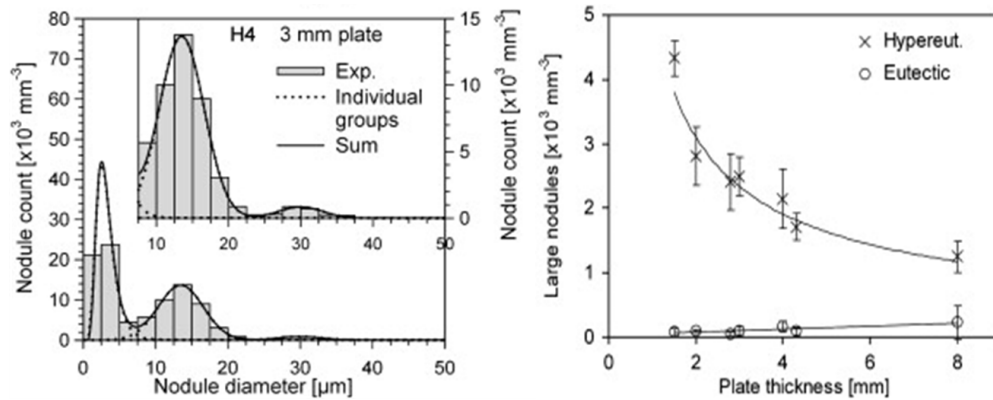
Figure 40 Nodule count and distribution statistics of hyper eutectic and eutectic ductile iron taken from the work of Pedersan et al (Pedersen and Tiedje 2008)

From these observation, the average initial defect size is assumed to be 15 microns. Hence for the Paris law model the assumption *a* =15 microns is taken and the a/c ratio is assumed to be a standard of 1.5. So, the initial value of '*c*' is 22.5 microns. Using these values an iterative calculation is run in MATLAB which calculates the shape function based on the values of *a* and *c* after each cycle and then updates the crack length too. The termination criteria of the calculation are if the value of *a* reaches the thickness of the plate or the value of *c* reaches the width of the plate.

57

4 Results

4.1 Fatigue and static analysis of differential

4.1.1 Stress contours in optimized differential

The figure below shows the stress contours in the normal direction $\sigma_x, \sigma_y, \sigma_z$ and $\tau_{xy}, \tau_{yz}, \tau_{zx}$. The maximum stress components are in the directions σ_z and τ_{zx} for both normal and shear components.
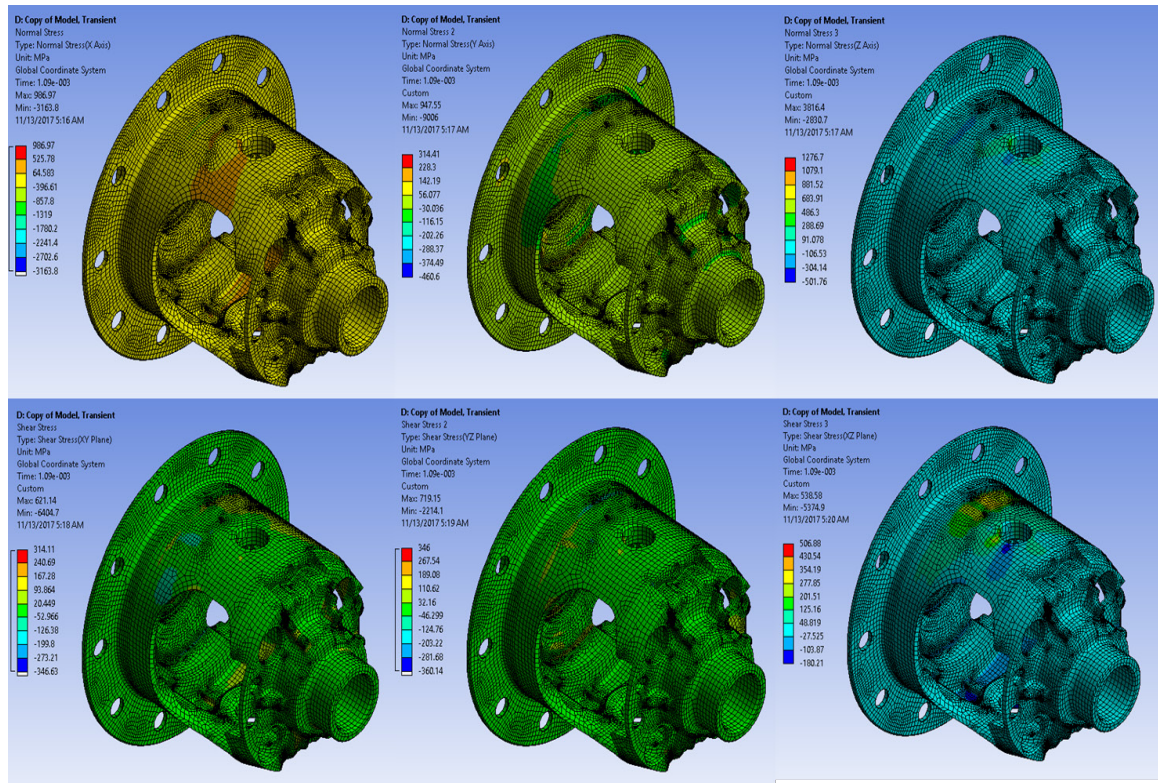
Figure 41 Stress contours for normal and shear stress components

The ANSYS static structural solver was used to generate these results. The stress values at all nodal locations were extracted in an Excel file for max and min step as described above. The calculations are for the alternating and mean stress tensors are done in Excel and the alternating and mean stresses are calculated. These values are then plotted on a Goodman diagram as shown in *Figure 42*. Similar diagrams were made for each load-step and the failure locations were identified.

58
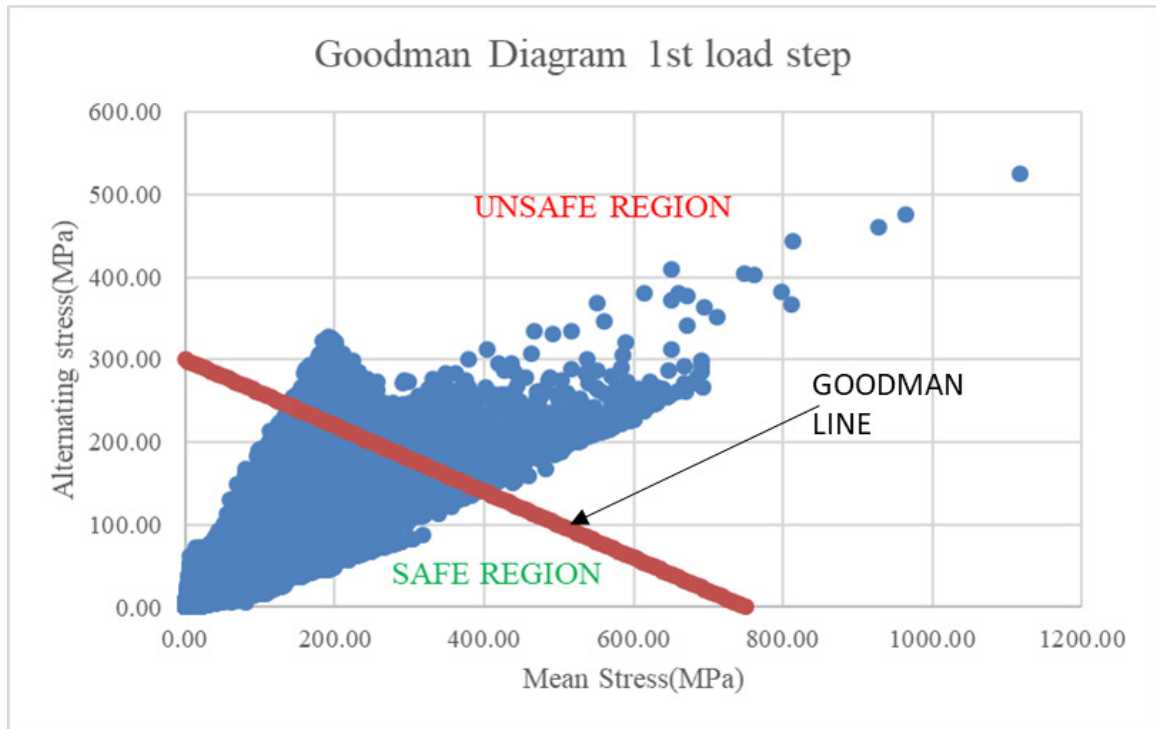
Figure 42 Goodman plot for 1st load case completion

The nodes lying in the unsafe region of the Goodman plot are identified by filtering the data in excel. The node number are then fed into ANSYS using the Named Selection dialog box. These node regions highlight distinct failure regions in the differential case. The cross-shaft region has been ignored from the results as per directions from EATON that the differential case is safe in that region. The *Figure 43* below shows the wireframe geometry highlighting the regions of failure identified from this method. The major areas of concern are found the stiffeners supporting both the cross-shaft regions, the sharp fillets in the window region of the differential and two areas in the bell region. These regions have been shown in detailed images as shown in *Figure 44*.

59
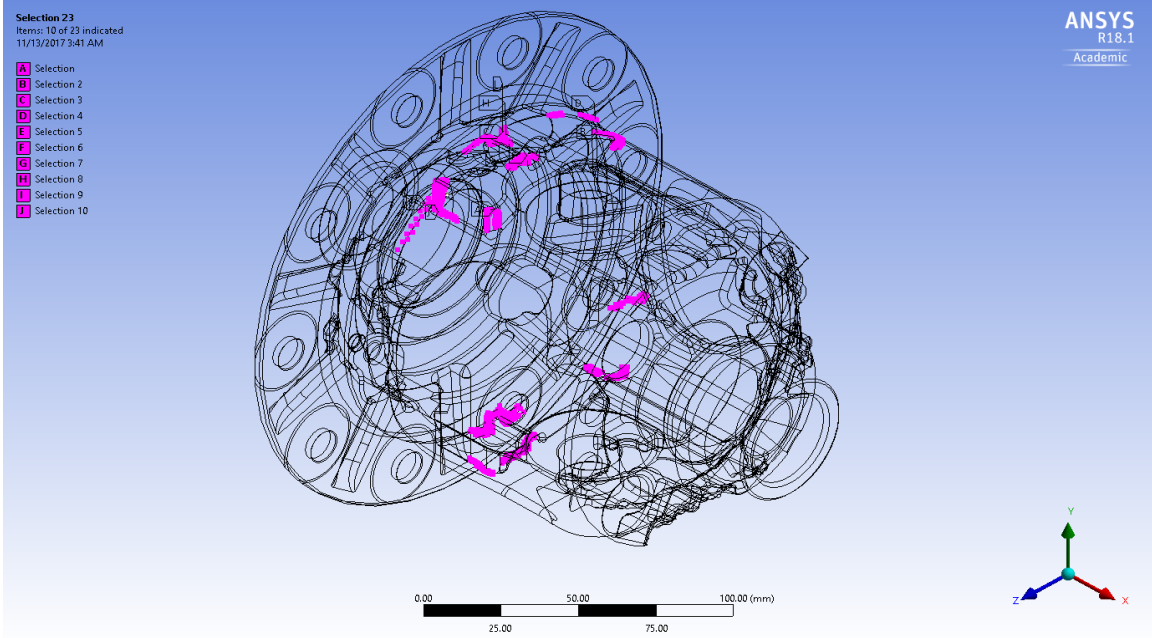
Figure 43 Regions of failure identified by Mason-McKnight method

Figure 44 Failure region details as calculated from the fatigue calculations (Clockwise going from top left to right: a) Left window and lower cross-shaft wall corner b) Right window and lower cross-shaft fillet corner c) Bell region internal fillets d) Upper cross-shaft stiffeners   e) Left window and upper cross-shaft fillets f) Barrel region between flange and left window)

60

4.1.1.1 FEA results with ANSYS transient structural solver

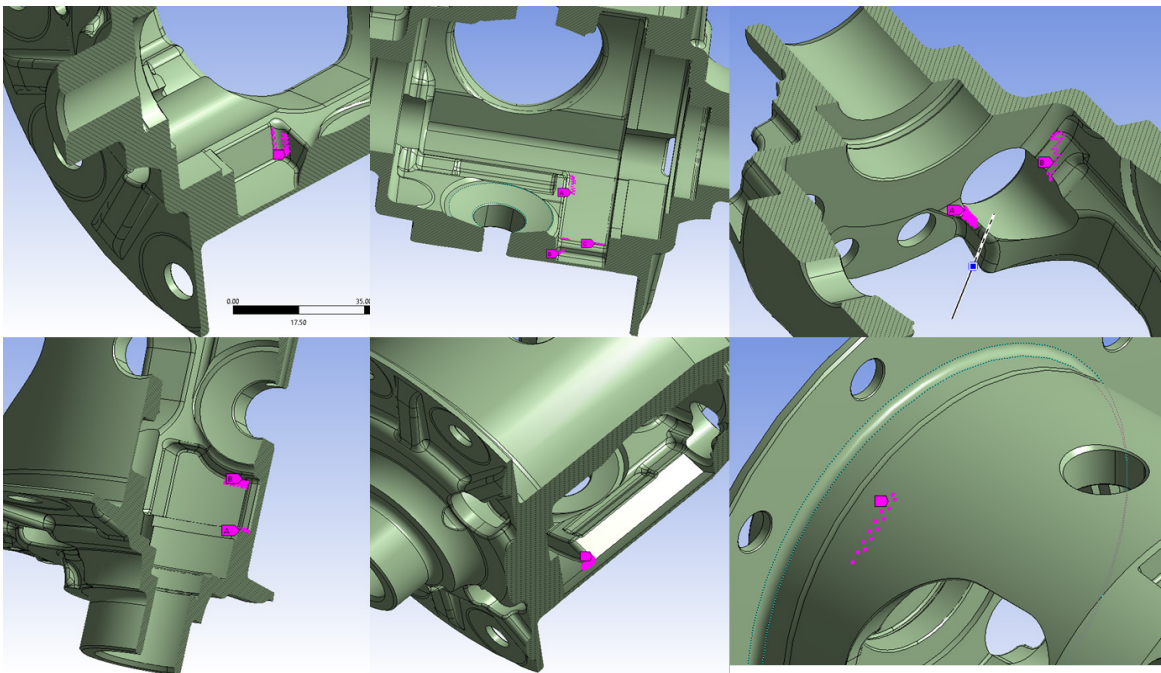The transient solver of ANSYS is a more exhaustive than the static solver and requires more computation time for the same simulation. Hence to compare the effect of solver selection only the first 6 load-steps were simulated in both the solvers. No real difference is observed in changing the solvers used to solve the same FE model. The equivalent von-Mises plots for both the solvers were found to be similar. The reason being as we are simulating a static case there is no inertial effect in the solution. Hence using a *Static Structural* solver for calculating equivalent alternating stresses is a better choice. However, in a dynamic FEA simulation where the effect of mass and inertia would be significant a transient solver should be used.

4.1.1.2 Geometry modifications in the differential

It was observed that the most critical regions were the stiffeners supporting the cross-shaft regions and the bell region damages. The geometry of the differential was then manually modified in SolidWorks 2017. The other regions are just above the margin of failure and could be attributed to a coarse mesh.3 mm of material was added on the stiffeners of the cross-shaft on both the locations. Figure below shows the comparison of the previous stiffeners to the added mass ones. The next figure shows the material added to the bell region identified as the failure area.
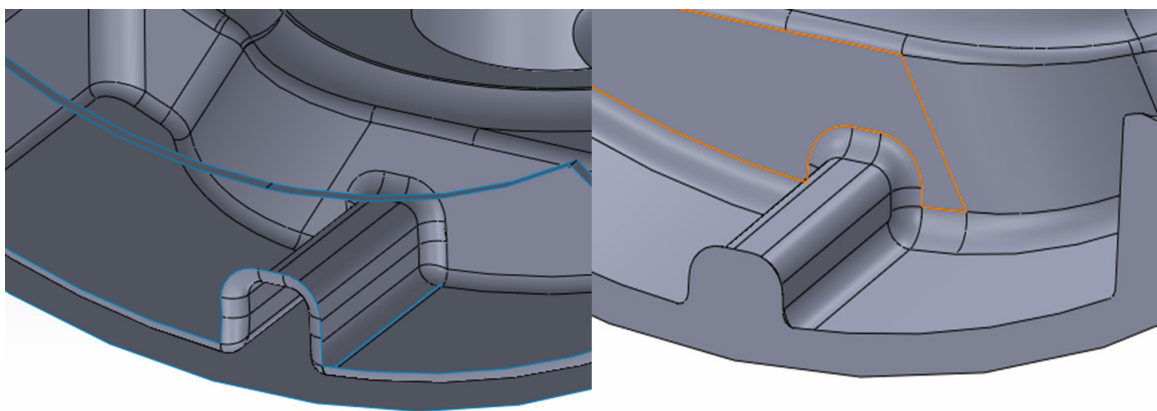
Figure 45 Thickness of the stiffeners increased to avoid failure
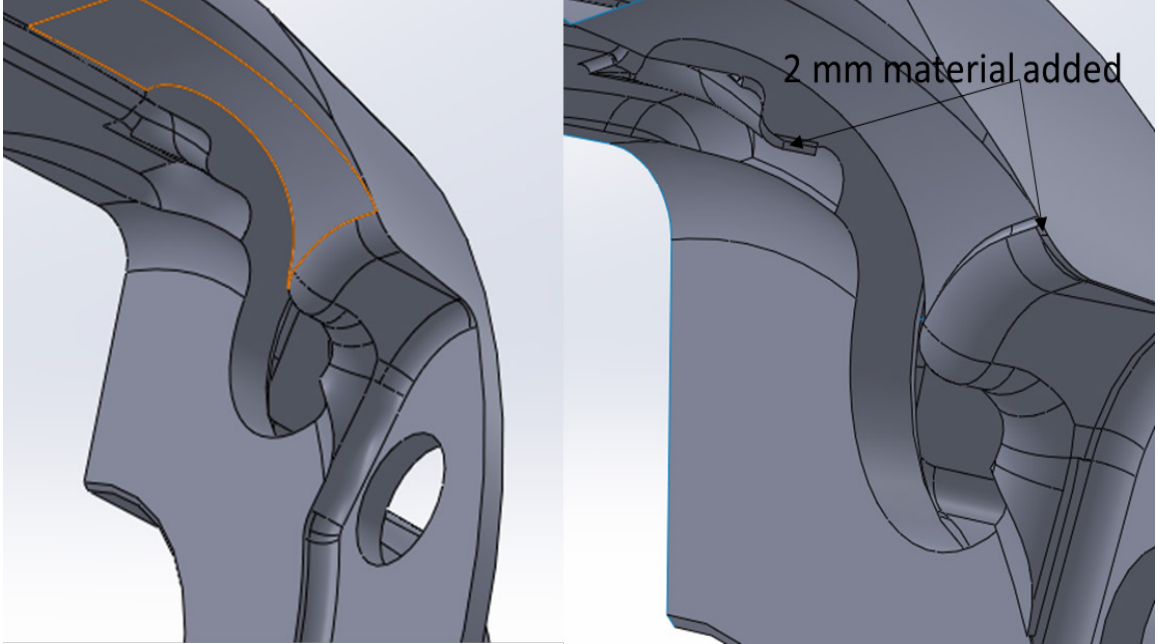
Figure 46 Material added in the bell region of the differential

4.1.1.3 Fatigue analysis of differential in Optistruct

The optimized differential design was analyzed for static and fatigue stresses in Optistruct. The results obtained were both static stress distribution and displacement. The fatigue module in Hypermesh does not give alternating stress results but only damage predictions in the model. Also, the material data on which damage predictions are based on assumptions to get the S-N curve of both the materials. *Figure 47* is the Von-Mises stress distribution for all 36 cases of load described earlier.
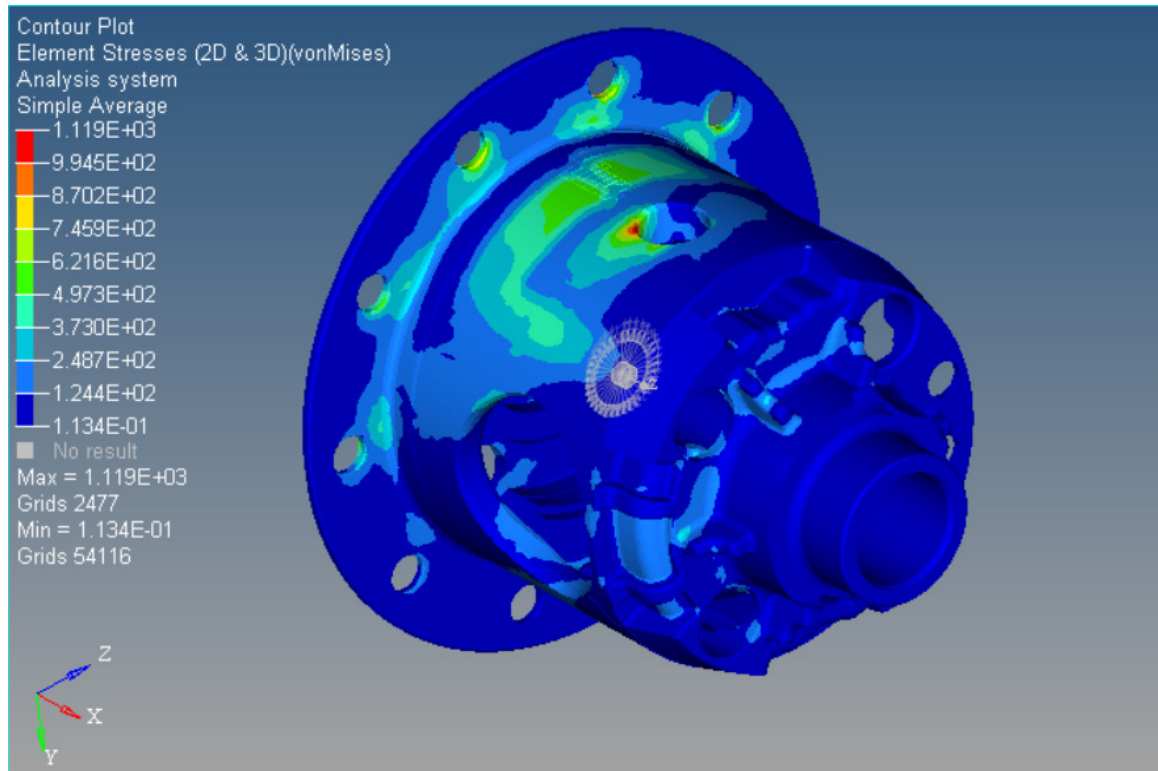
Figure 47 Equivalent Von-Mises stress distribution

The contour plots shown in *Figure 48* and *Figure 49* show the damage plot after repeated loading of the ring gear and pressure forces. The contour shows maximum damage on the rib sections used in the bell region of differential and the stiffeners in the cross-shaft.

63

Figure 48 Damage contour plot with all 36 load cases

Figure 49 Damage shown at similar locations as identified by modified MMK method

64

5   Conclusions

5.1 Fatigue Analysis of Differential Case

The fatigue analysis of differential case was carried out in three solvers

1. ANSYS Static structural solver
2. ANSYS Transient structural solver
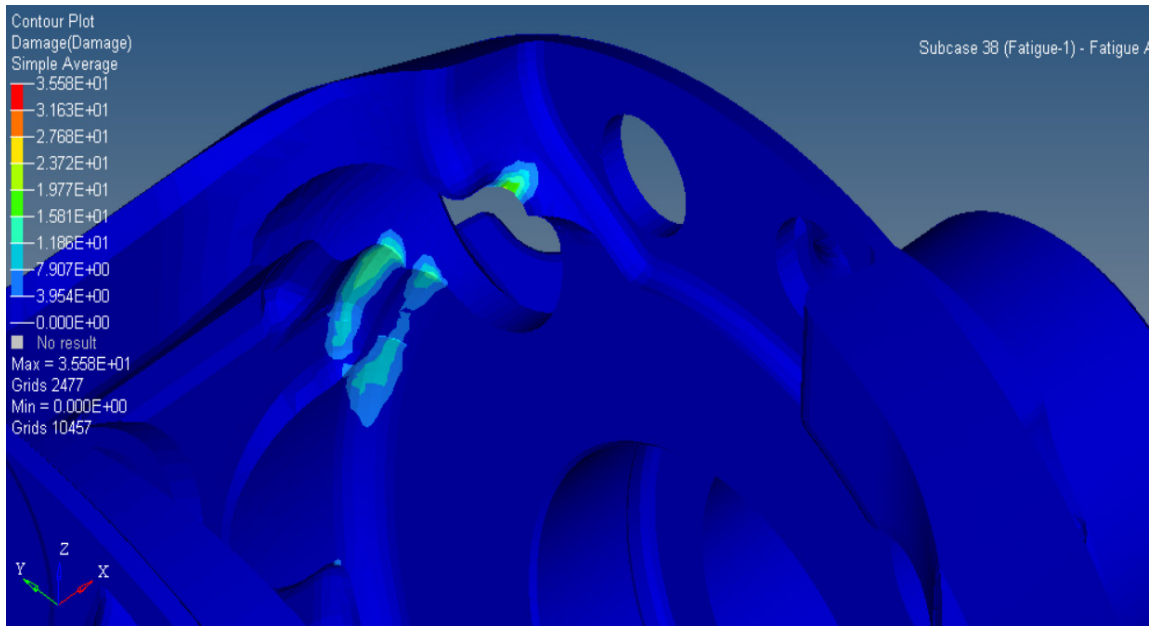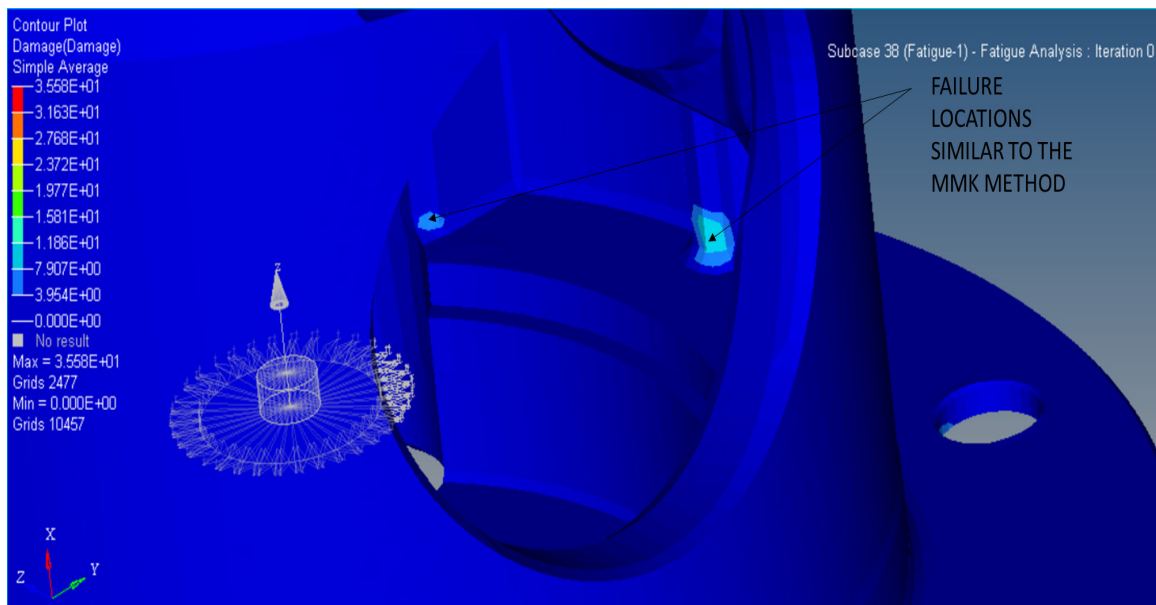3. Hypermesh solver

Both the ANSYS solvers were found to be a better choice for fatigue analysis by using static load-cases than Optistruct. Even without S-N data available alternating and static stress data can be extracted in a worksheet and conventional Goodman or Gerber techniques can be used to determine the failure regions.

Using these techniques and data in the Goodman diagram in *Figure 42* the critical regions identified are the stiffener ribs supporting the cross-shaft region. Also, the flange area needs to be strengthened near the flange and bearing block surface.

The damage results obtained from fatigue modelling in Optistruct show descent co-relation with the modified MMK technique used but with many assumptions like material S-N curve. Various combinations of alternating and static results were modelled to study the working of the fatigue solver for Optistruct. It has been observed that the solver code does not consider the effect of mean stress on fatigue life and damage of the component. This produces erroneous results and damage locations displayed can be different than physical loading.

5.2 Fatigue testing of ductile iron

Around 10 samples of the proposed geometry were tested in the flexural fatigue testing machine. It was observed that failure location is consistently obtained at the fillets where near the clamping fixtures of the sample. Also, the fracture surfaces showed very little plastic deformation and close to brittle behavior. The reason for this could that the

65

operating mechanism of the machine produces a very large strain in this narrow geometry. The observed fracture shown in *Figure 50* surface did not show ductile fracture characteristics and more of a fast brittle fracture. All the fracture surfaces show a possible crack initiation location but thereafter a fast fracture which appears like a brittle fracture. This can be due to the high strain being applied on the sample. The observations on effect of thickness on the stress shows that stress increases significantly when thickness is reduced. It can be concluded that a thinner cross-section with identical specimen design would be an ideal design as even small amounts of strain would result in large surface stresses.
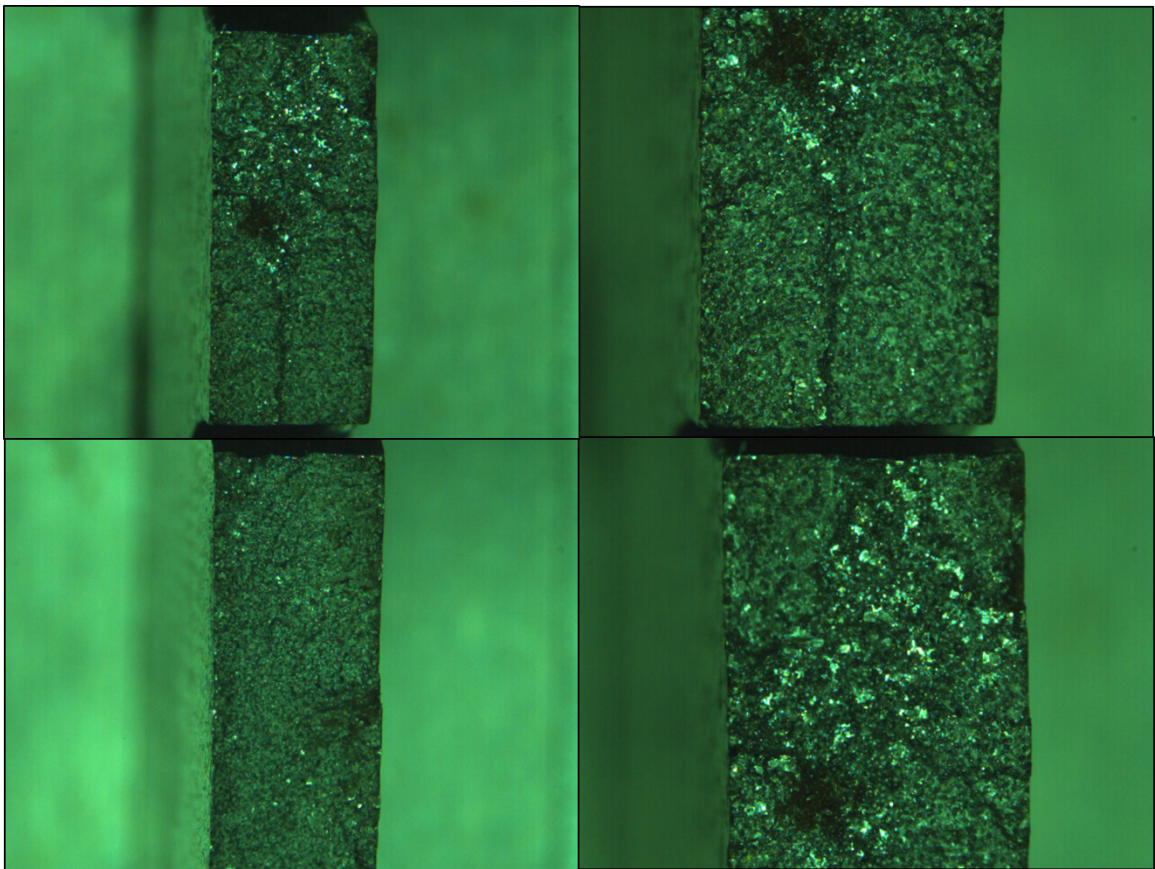
Figure 50 Fracture surface images of two specimens from each iteration of the sample design tested

A sample with more width and thin cross section would be an ideal one for this kind of testing. The test method is recommended to be changed to use samples of the same cross-

www.manaraa.com

section and width. A more standard metal fatigue test using a tension-tension loading of specimens needs to be adopted. Although the procedure is more time consuming and costly, it would help to localize the failure in desirable location on the sample. The test and specimen design for the new test has already been started.

The fracture mechanics model for predicting the crack propagation life is just a preliminary proposal and needs to be developed more comprehensively and validated as the testing progresses. Similar approaches need to be explored for other casting defects also and all these approaches can be combined to accurately predict the fatigue crack growth in ductile iron.

6   Bibliography

Deshpande, Parag. *DESIGN OPTIMIZATION PROCESS OF DIFFERENTIAL CASE.* Master's Report, Michigan Technological University, 2016.

Ductile Iron Society. *Ductile Iron Society.* 2013. http://www.ductile.org/didata/Section3/3part1.htm#Fatigue Limit (accessed 10 15, 2017).

Endo, M. "Effects of graphite shape, size and distribution on the fatigue strength of spheroidal graphite cast irons." *Metal Fatigue: effects of Small Defects and Nonmetallic Inclusions, Elsevier, J. SOC. Mater Sci. Jpn., 38(433)*, 1989: 1139-1144.

Heyes, A. M. "Automotive Component Failures." *Engineering Failure Analysis*, 1998: 129-141.

J. C. Newman Jr., I. S. Raju. "Stress intensity factor equations for cracks in three-Dimensional finite bodies." *NASA Technical Memorandum 83200*, 1981: 50.

Jan Papuga*, Miguel Vargas*, Martin Hronek*. "EVALUATION OF UNIAXIAL FATIGUE." *Engineering MECHANICS Vol 19*, 2102: 99-111.

Kalan, Pankaj N. *FINITE ELEMENT ANALYSIS AND TOPOLOGY OPTIMIZATION OF DIFFERENTIAL CASE AND CONTROL ARM FOR STATIC AND FATIGUE LOADING.* Master's Report, Michigan Technological University, 2016.

M. Dong, G. Hu, A. Diboine, D. Moulin, C. Prioul. "Damage modelling in nodular cast iron." *Journal de Physique IV Colloque,*, 1993: 643-648.

M.Suraratchai, J.Limido, C.Mabru, R.Chieragatti. "Modelling the influence of machined surface roughness on the fatigue life of aluminium alloy." *International Journal of Fatigue*, 2008: 2119-2126.

Matteo Benedetti, Elisa Torresani, Vigilio Fontanari and Danilo Lusuardi. "Fatigue and Fracture Resistance of Heavy-Section Ferritic Ductile Cast Iron." *Metals*, 2017: 88-107.

Mhapankar, Mayur. *Weight Reduction Technologies in the Automotive Industry.* Thematic, Aranca, 2015.

Paul Kainzinger, Christoph Guster,Martin Severing, Anton Wolf. "Influence of micro-shrinkage on the fatigue behavior of ductile iron." *13th International Conference on Fracture* . Beijing, China: Elsevier, 2004. 311-319.

Pedersen, Karl Martin, and Niels Skat Tiedje. "Graphite nodule count and size distribution in thin-walled ductile cast iron." *Materials Characterization, 59(8),*, 2008: 1111-1121.

Reinl, Alexander D. *Effects of Cooling Rate and Alloy Chemistry on Microstructure and Mechanical Properties on Thin Wall Ductile Iron.* Thesis, Houghton: Michigan Technological University, 2016.

S Boonmee, D. M. Stefanscu. "Effect of Casting Skin on Fatigue Properties of CG Iron." *International Journal of Metalcasting*, 2016: 15-26.

S Boonmee, D. M. Stefanscu. "Occurrence and effect of casting skin in compacted graphite iron." *International Journal of Cast Metals Research*, 2016: 47-54.

S. Boonmee, B. Gyesi, D. M. Stefanescu. "Casting Skin of Compacted Graphite Iron." *American Foundry Society*, 2010: 1-12.

S. Sreedhar, D. Marla, D. Guo. "Fatigue Analysis for Axle Differential Cases." *SAE TECHNICAL PAPER SERIES*, 2006: 6.

S.K. A ° sa, *, B. Skalleruda, B.W. Tveitenb, B. Holmeb. "Fatigue life prediction of machined components using finite." *International Journal of Fatigue 27*, 2005: 1590-1596.

Y.Nadota, J.Mendeza, N.Ranganathan. "Fatigue life assessment of nodular cast iron containing casting defects." *Fatigue & Fracture of Engineering Materials & Structures*, 2001: 289-300.

Yue Cui Hui-qing Lan, Ren-yang He, Chao-hui Zhang. "Flow-field stress intensity exceeds simple pressure load at defect - Oil & Gas Journal." *Oil & Gas Journal.* 01 06, 2014. http://www.ogj.com/articles/print/volume-112/issue-1/transportation/flow-field-stress-intensity-exceeds-simple.html (accessed 08 01, 2017).

Zhao, Wei LiuEmail authorWei-hao ZhaiJun-feng. "Influence of shrinkage porosity on fatigue performance of iron castings and life estimation method." *China Foundry*, 2016: 47-53.

Eaton (2015). MLD Case - FEA.

Klipfel, D. (2016). Differential case assembly.
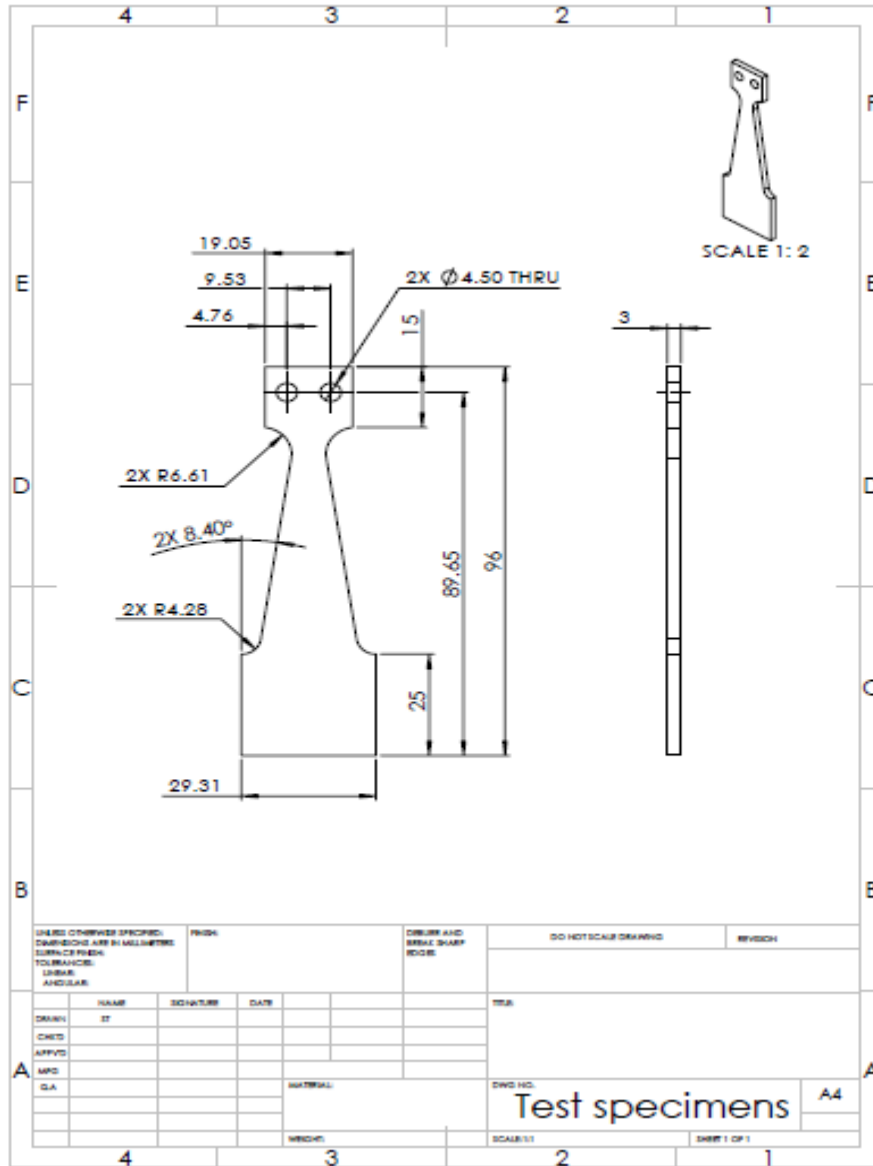
A   Drawings of flexural fatigue samples
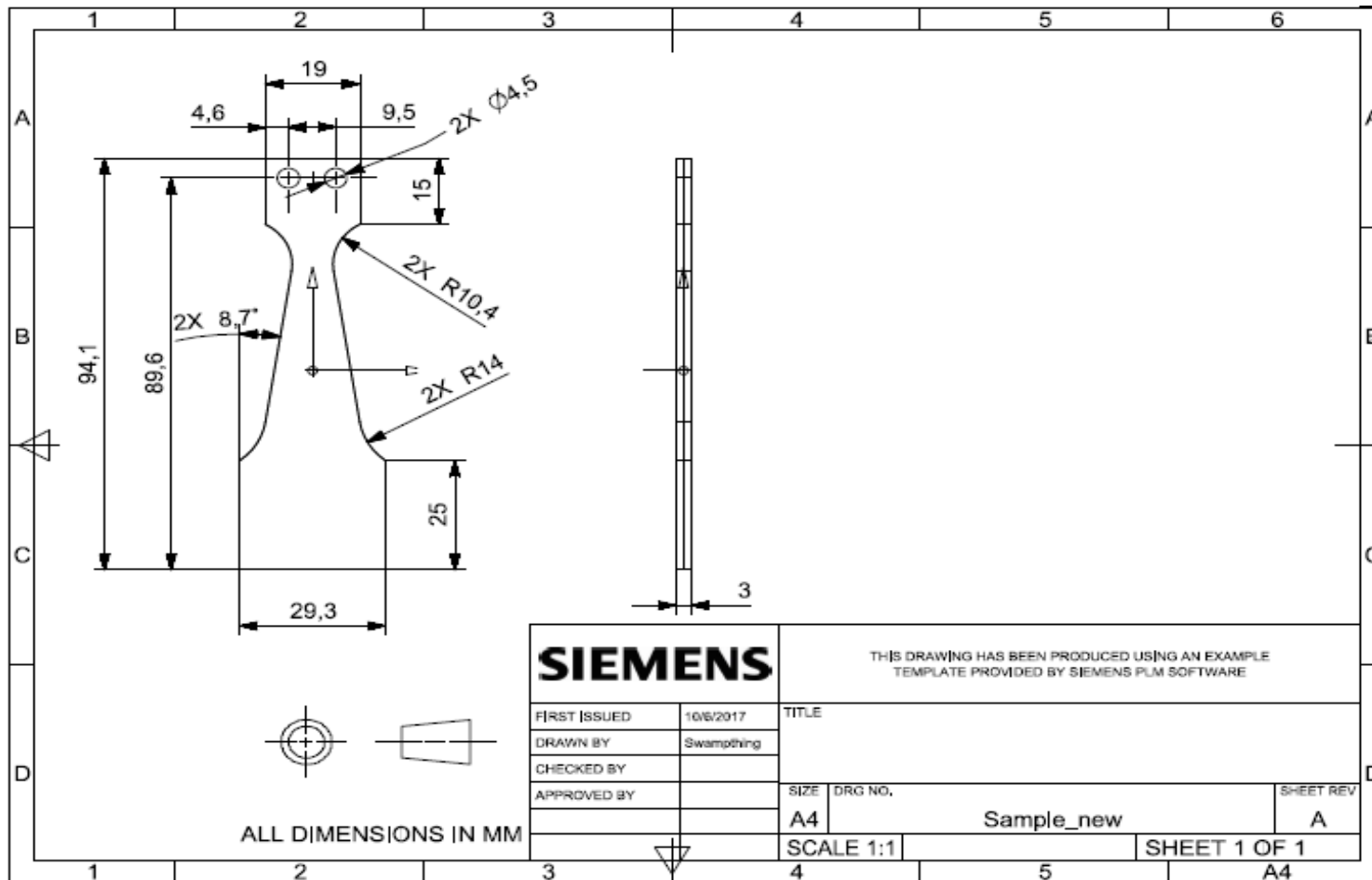

Figure 51 Manufacturing drawing for first sample design

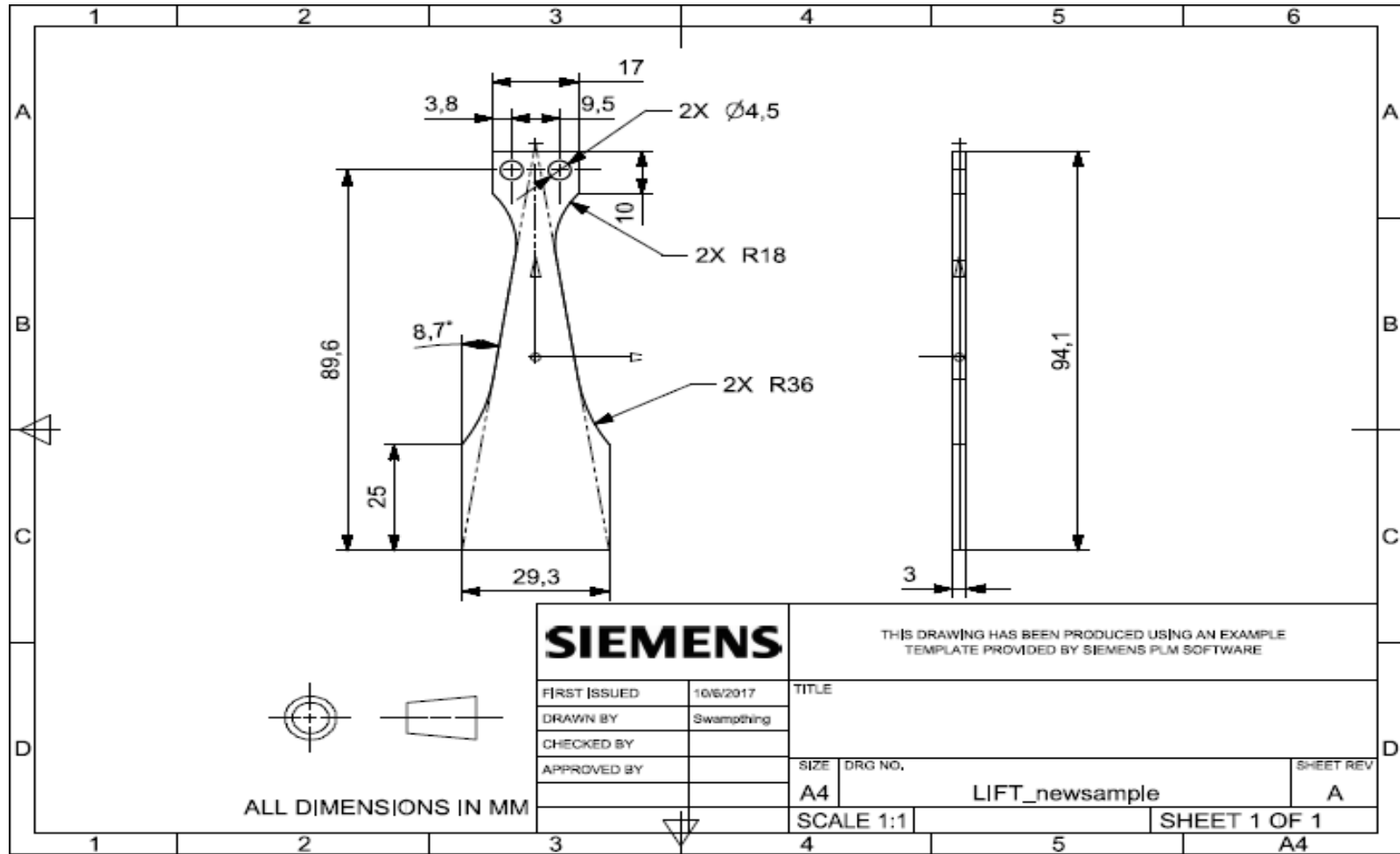*Figure 52 Manufacturing drawing for first iteration of sample design*

Figure 53 Manufacturing drawing for final iteration of sample design

72